BRITISH COLUMBIA
est. 1895
GEOLOGICAL SURVEY

Remotely piloted aircraft system (RPAS) for investigating surface sediments in the Interior Plateau of British Columbia: Methods, data, and products

E.A. Elia
T. Ferbey
B.C. Ward
R.B.K. Shives
M. Best
N. Martin-Burtart

BRITISH COLUMBIA
Ministry of
Energy, Mines and
Low Carbon Innovation

GeoFile 2023-07

Ministry of Energy, Mines and Low Carbon Innovation
Mines, Competitiveness, and Authorizations Division
British Columbia Geological Survey

Recommendation citation: Elia, E.A., Ferbey, T., Ward, B.C., Shives, R.B.K., Best, M., and Martin-Burtart, N., 2023. Remotely piloted aircraft system (RPAS) for investigating surface sediments in the Interior Plateau of British Columbia: Methods, data, and products. British Columbia Ministry of Energy, Mines and Low Carbon Innovation, British Columbia Geological Survey GeoFile 2023-07, 22 p.

Front Cover:
Hardware used to complete magnetic, radiometric, lidar, and aerial photography surveys. Photograph taken using a DJI Mini 2 RPAS flying 10 m above ground level. **Photo by Travis Ferbey**.

Back cover:
Ground station for RPAS surveys. In background, DJI Matrice 600 Pro aircraft mounted with an RS-530 gamma-ray spectrometer. Photograph taken using a DJI Mini 2 RPAS flying 5 m above ground level. **Photo by Travis Ferbey**.

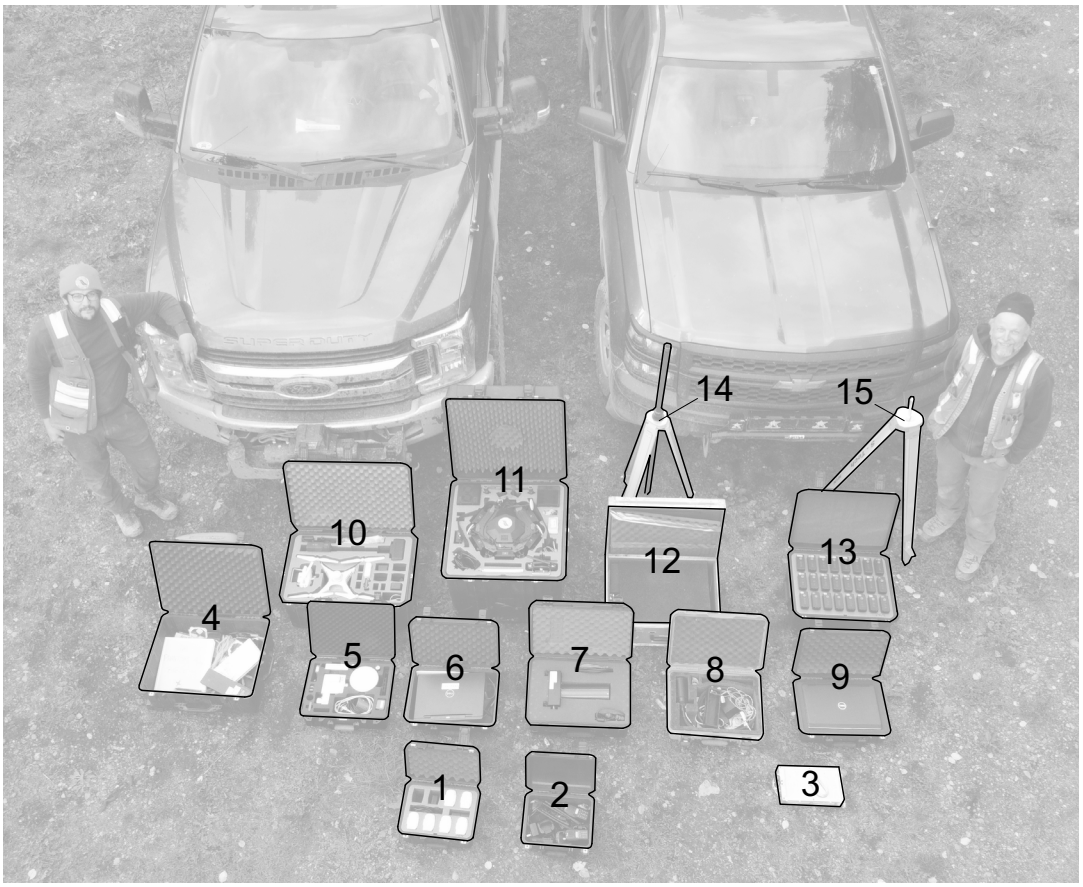

1. DJI Phantom 4 RTK batteries, **2.** air-band handheld VHF radios, **3.** magnetometer mount for DJI Matrice 600, **4.** tools, VFR navigation charts, and manuals, **5.** GreenValley International LiAir V70 lidar and base station, **6.** laptop running GreenValley International LIDAR360 and LiGeoreference software, **7.** Radiation Solutions Incorporated RS-530, **8.** GEM Systems DRONEmag magnetometer, **9.** laptop running SPH Engineering UgCS flight planning software, **10.** DJI Phantom 4 RTK and base station, **11.** DJI Matrice 600 Pro, **12.** GEM Systems (base station) magnetometer, **13.** DJI Matrice 600 Pro batteries, **14.** RTK base station tripod, and **15.** lidar base station tripod.

BRITISH COLUMBIA | Ministry of Energy, Mines and Low Carbon Innovation

Remotely piloted aircraft system (RPAS) for investigating surface sediments in the Interior Plateau of British Columbia: Methods, data, and products

E.A. Elia
T. Ferbey
B.C. Ward
R.B.K. Shives
M. Best
N. Martin-Burtart

Ministry of Energy, Mines and Low Carbon Innovation
British Columbia Geological Survey
GeoFile 2023-07

Remotely piloted aircraft system (RPAS) for investigating surface sediments in the Interior Plateau of British Columbia: Methods, data, and products

E.A. Elia[1,2], T.Ferbey[1], B.C. Ward[2], R.B.K. Shives[3], M. Best[4], and N. Martin-Burtart[5]

[1] British Columbia Geological Survey, Ministry of Energy, Mines and Low Carbon Innovation, Victoria, BC, V8W 9N3
[2] Department of Earth Sciences, Simon Fraser University, Burnaby, BC, V5A 1S6
[3] GamX Inc., Kanata, ON, K2L 3Z8
[4] Bemex Consulting International, Victoria, BC, V9C 4M7
[5] Radiation Solutions Inc. Mississauga, ON, L4Z 2H4
[a] corresponding author: easton.elia@gov.bc.ca

Recommendation citation: Elia, E.A., Ferbey, T., Ward, B.C., Shives, R.B.K., Best, M., and Martin-Burtart, N., 2023. Remotely piloted aircraft system (RPAS) for investigating surface sediments in the Interior Plateau of British Columbia: Methods, data, and products. British Columbia Ministry of Energy, Mines and Low Carbon Innovation, British Columbia Geological Survey GeoFile 2023-07, 22p.

Abstract

Recent advancements in remotely piloted aircraft systems (RPAS) and the miniaturization of external sensors have made collecting geomatics, geological, and geophysical data more accessible. These data can be affordably acquired at spatial resolutions similar to traditional fixed-wing and helicopter-mounted surveys, in some instances at higher resolutions, and can be visualized and used in near-real time. In the 2021 and 2022 field seasons, we used RPAS aircraft to collect gamma-ray spectrometer, magnetometer, and lidar data and aerial photographs for photogrammetric processing at 13 sites centred on alkalic and calc-alkaline porphyry systems in the Mount Polley mine, Woodjam prospect, and Guichon Creek batholith areas of the Interior Plateau. Because glacial deposits cover bedrock in large parts of the Interior Plateau, the surveys were designed to assess the application of RPAS-borne instruments for mapping surficial geology and to test their use for drift prospecting of subglacial tills in areas and of known mineralization. Magnetic and radiometric data were collected over areas of 10000 m2 at a 5-10 m line spacing and a 5-10 m instrument height that was maintained using an RPAS-mounted altimeter and active terrain-following software. Data processing techniques, developed for use in the field with a laptop, produced images of gridded magnetic total field, magnetic first vertical derivative, radioelement concentrations (K, eU, eTh), and radioelement ratios (eTh/K, eU/eTh, and eU/K), with a cell size resolution of 1.67 to 3.33 m. Lidar data were collected at 80-100 m above take-off elevation at a 90-110 m line spacing to produce bare-Earth digital elevation models (DEM) with a cell size resolution of 0.5-0.25 m. Aerial photographic surveys used an RPAS-fixed RGB camera flying 80 to 100 m above take-off location with data being processed in the field using the structure from motion technique, to obtain cm-scale resolution DEMs and orthomosaic images. In this report, we summarize the RPAS platforms and sensors we used in 53 individual surveys, describe the methods for acquiring and processing survey data and, in an accompanying supplementary file, release raw and processed magnetic and gamma-ray spectrometry radiometric data and lidar and air photo products.

Keywords: remotely piloted aircraft system, magnetometer, gamma-ray spectrometer, lidar, photogrammetry, radiometrics, digital elevation model

1. Introduction

The use of remotely piloted aircraft systems (RPAS) in geoscience has quickly expanded from a novel method primarily to take perspective photos and videos, to a practical data acquisition tool. User-friendly commercial RPAS hardware and software are now available to design and implement surveys using many different sensors such as lidar, magnetometers, gamma-ray spectrometers, electromagnetics, hyperspectral cameras, and gas detectors (Chabot, 2018; Aleshin et al., 2020). Additional studies have explored the possibility of mounting ground penetrating radar, seismic, and gravity instruments for RPAS-borne data acquisition (Weiner et al., 2020; Tsuji et al., 2021; Francke, 2022). Compared to traditional fixed-wing airplanes and helicopters, these systems are affordable, versatile, and can be flown with minimal training. Nonetheless, the rapid development of RPAS instruments has led to uncertainty surrounding their products and the mineral exploration industry continues to rely on long-standing traditional fixed-wing and helicopter-mounted platforms.

Drift prospecting is a mineral exploration technique that uses the composition of glacial sediments to infer bedrock source lithology and location (e.g., McClenaghan and Paulen, 2017). Till geochemistry and mineralogy surveys are specific drift prospecting techniques that analyze the matrix (<2.0 mm fraction) of subglacial tills. If these tills have a predictable transport history and are considered to be a first derivative

of bedrock, they may be used to infer the geochemical and mineralogical properties of an up-ice bedrock source (McClenaghan et al., 2013). Dispersal trains in till present an ideal exploration target because the geochemical and/or mineralogical anomaly can be many times larger than the bedrock source (McClenaghan and Paulen, 2017). Till surveys have been used extensively in glaciated terrains, particularly in the Interior Plateau of British Columbia (Fig. 1) where bedrock is commonly buried beneath thick drift cover, both as a test of known sources of copper-gold-molybdenum mineralization (Hashmi et al., 2015b; Plouffe and Ferbey, 2016), and to discover new sources (Ney et al., 1972; McClenaghan and Paulen, 2017). Importantly, both magnetite grains in till (Pisiak et al., 2014; Sappin et al., 2014) and detectable anomalies in airborne gamma-ray spectrometry data over tills (Ford et al., 1988) have been used to identify dispersal from mineralized source rock.

From 2019 to 2022, we implemented a project to assess the application of RPAS for surficial geology mapping and drift prospecting. The project began with a small, consumer quadcopter RPAS to help guide surficial geology mapping in north-central British Columbia (Elia and Ferbey, 2019). The data acquired from this program allowed us to map glacial landforms and investigate geologic contacts (bedrock and surficial) that could not be observed in traditional analysis of satellite or aircraft-acquired images (Elia and Ferbey, 2019; Ferbey and Elia, 2020). We saw the potential for these systems to collect data at a scale between traditional airborne surveys and ground observations. We also identified other data types that could potentially contribute to future drift prospecting programs. From here, the project evolved to using a larger hexacopter RPAS with geophysical payloads to assess the utility of RPAS-borne sensors to map and characterize the composition of surficial sediments in areas of known mineralization in the Interior Plateau. The objectives of the current project are to: 1) assess the application of commercially available RPAS systems, sensors, and software to geoscience data collection; 2) validate RPAS magnetic and radiometric survey results using traditional airborne (magnetics, radiometrics) and ground (till sampling, soil sampling, magnetic susceptibility, radiometrics) data; and 3) determine if low-altitude, terrain-following magnetic and radiometric data can identify dispersal trains in subglacial tills by mapping differences in sedimentology, geochemistry, and mineralogy.

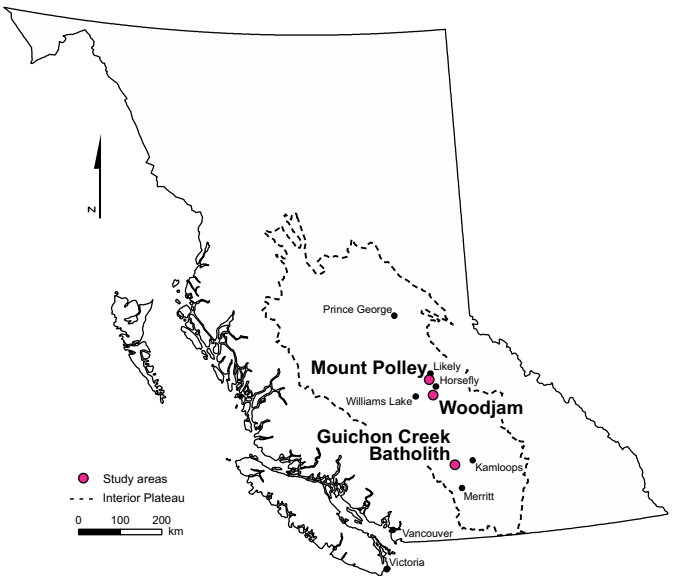

Fig. 1. Study area locations. Pink circles indicate porphyry occurrences where we based our field operations. The dotted line shows the extent of the Interior Plateau.

Our surveys centred on tills derived from porphyry systems in the Mount Polley mine, Woodjam prospect, and Guichon Creek batholith areas of the Interior Plateau (Fig. 1). We flew 53 autopilot surveys at 13 sites over subglacial tills derived from known alkalic and calc-alkaline porphyry deposits using RPAS-mounted radiometric, magnetic, and lidar instruments and a purpose-built RPAS used to collect aerial photographs for photogrammetry. Because mineralization in porphyry deposits tends to be spatially related to alteration and resulting K enrichment, measuring gamma radiation from the decay of the radiogenic ^{40}K isotope with a gamma-ray spectrometer can be used as an effective exploration tool to identify near-surface K. Similarly, because porphyry deposits commonly contain modified magnetite concentrations, a magnetometer may help identify down-ice dispersal of glacially eroded deposits. We also collected lidar data and aerial photographs to map surficial geology, interpret ice-flow history, and identify areas for till sampling.

In this report, we summarize the RPAS platforms and sensors we used, describe the methods for acquiring and processing survey data and, in the accompanying supplementary file <BCGS_GF2023-07.zip>, release raw and processed magnetic and gamma-ray spectrometry radiometric data and lidar and air photo products. Validation and interpretation of our RPAS geophysics data will be the focus of future publications.

2. Review: RPAS aerial photography, lidar, magnetometry, and gamma-ray spectrometry

2.1. Aerial photography and lidar

The structure-from-motion (Sfm) photogrammetric technique identifies common points in adjacent, overlapping, geolocated air photos and places these points in three-dimensional space to build point clouds that are used to create models of the ground surface (Johnson et al., 2014; Elia and Ferbey, 2019). These models can be further manipulated to derive bare Earth digital elevation models (DEM) and orthomosaic imagery. RPAS photogrammetry techniques most commonly use air photos acquired from a red-green-blue (RGB) camera mounted to the aircraft. Geologists can use RPAS-derived photogrammetry products to: supplement base maps used in large-scale mapping projects (Honarmand and Shahriari, 2021; Spence et al., 2022); interpret the genesis and composition of glacial landforms (Elia and Ferbey, 2019; Ferbey and Elia, 2021); identify rock type and measure unit thicknesses, bedding, and structures to construct outcrop models and detailed stratigraphic logs (Vollgger and Cruden, 2016; Nesbit et al., 2018; Smith and Maxwell, 2021).

Similar products with similar applications can be built from light detection and ranging (lidar) data. Lidar instruments construct three-dimensional point clouds by measuring the travel time of reflected laser light between the instrument and an object. They have a wide field of view (up to 180°, resulting

in oblique returns) and emit coherent, tightly focused, and in-phase pulses of laser light at high frequency (up to 250 kHz) for long distances (Lemmens, 2007; Lohani and Ghosh, 2017; Nayegandhi and Nimetz, 2018). This light can be reflected by the Earth's surface or objects that obscure it. In heavily forested areas where multiple returns define the tree canopy, filtering a lidar point cloud's early returns and using only last returns produces a DEM that represents the Earth's surface (called a bare-Earth model) (Maune et al., 2018).

Lidar is an invaluable tool for producing digital models of bedrock outcrop, 3-dimensional geologic mapping, and stratigraphic analyses (Bellian et al., 2005; Sahoo and Gani, 2015). Lidar DEMs have been applied throughout western North America to identify and interpret glacial landforms (Demchuk et al., 2005), monitor geohazards (Bonneau and Hutchinson, 2019), and serve as a base for geological maps and traverse planning (Haugerud et al., 2003).

2.2. Magnetometry

Magnetometry is the measurement of lateral changes in the Earth's ambient magnetic field. A magnetometer measures these variations by sensing differences in the magnetic susceptibility of the underlying ground. In geoscience, these changes are largely related to mineralogy, specifically the presence and abundance of magnetite, but also pyrrhotite and hematite (Telford et al., 1989).

Magnetometers are the most widely adopted RPAS-borne geophysical sensor for mineral exploration. Most drone magnetometers are optically pumped potassium vapour or cesium vapour models. These models detect changing magnetic intensity by measuring the transparency of vapour within the instrument, related to the measured magnetic field (e.g., Telford et al., 1989). Vapour magnetometers allow sensitive (0.0002 nT) and precise measurements of magnetic field intensity (Total Magnetic Intensity or TMI in nT) and, at less than 2.0 kg, are easily towed by commercially available RPAS. Other scalar and fluxgate vector magnetometers exist for RPAS applications and have been applied to a range of geophysical problems (Le Maire et al., 2020).

Magnetometers carried by an RPAS can collect geologically meaningful results at a range of heights, with the flight height, line spacing, and sample frequency ultimately determining ground resolution (Le Maire et al., 2020). Low altitude (5 to 30 m above ground level) RPAS magnetic surveys have identified new mineralized zones that were undetectable in traditional airborne data (Walter et al., 2010), including iron-oxide mineralization specific to magnetite and hematite deposits (Malehmir et al., 2017), and have located buried metallic objects including pipes (Le Maire et al., 2020) and unexploded ordinance (Kolster et al., 2022). The total magnetic field can be further processed to generate other products, such as reduction to the pole, derivatives, and high and low pass filters, that can be used to separate shallow from deeper magnetic features (Nabighian, 2005).

2.3. Radiometrics by gamma-ray spectrometry

Gamma-ray spectrometers measure gamma-ray emissions (in counts per second) within specific energy windows, which are used to calculate radioelement concentrations (Telford et al., 1989). The radioelements potassium, uranium, and thorium commonly occur in rock-forming minerals and so their concentrations (% and ppm) can be used to investigate the composition of bedrock and surficial sediments (Telford et al., 1989; Porter and Lowe, 2000; Shives et al., 2000; Shives, 2015). However, O'Reilly and Ford (1988) noted that the thickness and provenance of till must be well understood to correlate a radiometric response to bedrock geology. Gamma-ray spectrometry (or radiometrics) is considered a surface geophysical technique because measurable gamma-ray emissions originate in the top 30 cm of the Earth's surface. These emissions can be measured on the ground (using a handheld instrument) or from the air (using an aircraft-mounted instrument). Radiometrics is a well-established technique for mapping geological contacts (e.g., Graham and Bonham-Carter, 1993), differentiating soil types and textures (Dent et al., 2013; Maino et al., 2022), and identifying specific rock types (O'Reilly and Ford, 1988). In some instances, airborne radiometrics can be used to differentiate post-magmatic metasomatism and hydrothermal alteration spatially associated with mineralization (O'Reilly and Ford, 1988; Shives et al., 2000; Shives, 2015). Along with their fixed-wing and helicopter-borne counterparts, low-altitude RPAS-mounted gamma-ray spectrometers, using significantly lower-volume crystals, have detected radioactive element anomalies related to clay and sand concentrations (van der Veeke et al., 2021), legacy Cu-Fe prospects (Martin et al., 2015, 2020) and uranium occurrences (Šálek et al., 2018), at higher spatial resolutions than traditional airborne surveys.

Noise-adjusted singular value decomposition (NASVD) filters are commonly applied to radiometric data to reduce noise and therefore highlight geologically meaningful information (Hovgaard and Grasty, 1997; Minty and Hovgaard, 2002). Error for each radioelement measurement is equal to the square root of counts recorded within the element's energy window, which is related to the radioactivity of the source, dimensions/volume of the detector, and measurement duration (Tammenmaa et al., 1976). Increasing each of these factors results in higher count rates and inherently less error. For airborne radiometrics surveys, many of these factors cannot be changed and altering them may result in lower spatial resolutions and/or smaller survey areas (Tammenmaa et al., 1976). The reduction of noise using the NASVD process is equivalent to increasing the instrument's detector volume by 3 or 4 times, thereby artificially increasing the counts and decreasing errors (Hovgaard and Grasty, 1997). With a NASVD filter, a user manually rejects high-noise components, generating a gamma-ray spectrum with approximately 50% less error and an increased reliability of radiometric data for geological studies (Minty and McFadden, 1998). NASVD is extremely effective for small-volume RPAS instruments, where scintillator size is generally limited.

3. Setting

We conducted RPAS surveys in three areas of the Interior Plateau (Fig. 1; Holland, 1976) where subglacial tills are common and bedrock outcrop is limited. The surveys were flown over subglacial tills down-ice of: 1) the Mount Polley mine (alkaline porphyry Cu-Au); 2) the Woodjam prospect (alkaline to calc-alkalic porphyry Cu-Mo-Au); and 3) parts of the Guichon Creek batholith, which hosts the Highland Valley Copper mine (calc-alkalic porphyry Cu-Mo), and numerous other porphyry occurrences.

3.1. Bedrock geology

The Interior Plateau is underlain by Quesnel terrane, an upper Paleozoic to lower Mesozoic arc assemblage of volcanic, intrusive, and sedimentary rocks (Logan and Mihalynuk, 2014). Quesnel terrane's Late Triassic to Early Jurassic intrusive complexes host many of British Columbia's porphyry deposits including alkalic Cu-Au mines at Mount Polley, Mount Milligan, Copper Mountain, and New Afton, and calc-alkaline Cu-Mo mines at Gibraltar and Highland Valley Copper (Clarke et al., 2023). The geology of Quesnel terrane is not well understood in areas where thick sections of glacial sediments (including subglacial tills) obscure bedrock.

3.1.1. Mount Polley mine

The Mount Polley alkalic porphyry Cu-Au deposit is hosted by the Mount Polley intrusive complex (Late Triassic), a suite of diorites to monzonites that cut stratified Nicola Group (Upper Triassic) volcanic and sedimentary rocks (Fig. 2; Rees, 2013; Brown et al., 2016). Mineralization is primarily in hydrothermal breccias and adjacent stockwork veins in the Springer, Cariboo, and Northeast-Boundary zones. Potassic and calc-potassic alteration and resultant K-feldspar enrichment throughout the deposit may coincide with magnetite-cemented breccias. In the Springer-Cariboo zone, copper mineralization is primarily chalcopyrite with minor bornite, which can be disseminated or concentrated in veins and breccia cements. The Northeast-Boundary zone has higher-grade zones of chalcopyrite and bornite in coarser breccia cements and veins. The breccia cement is also enriched in gold. However, in the Northeast zone, gold is more commonly held in pyrite than in the copper sulphides, with bornite containing no gold or silver (Rees, 2013; Brown et al., 2016). Post-intrusion cover rocks include Kamloops Group (Early Tertiary) volcanic and sedimentary rocks and Ashcroft Formation (Tertiary) sandstones and conglomerates (Logan et al., 2010). The Mount Polley intrusive complex is easily identified within regional-scale airborne magnetics and radiometrics data (Shives et al., 1995, 2004).

3.1.2. Woodjam prospect

The Woodjam prospect is on the northern margin of the Takomkane batholith (Early Jurassic) a calc-alkaline body that intrudes Nicola Group (Early Jurassic) volcanic and volcanosedimentary rocks (Fig. 2; Sherlock et al., 2013; Laird, 2017). North of the batholith, the Deerhorn, Megabuck, Takom, Three Firs, and Spellbound mineralized zones are near the contacts of satellite intrusions; the Southeast zone is in the main batholith (Fig. 2). The Woodjam prospect is unique in that it potentially hosts both alkalic (Deerhorn, Megabuck) and calc-alkaline (Takom, Three Firs, Spellbound, Southeast zone) styles of porphyry mineralization. Throughout the prospect, mineralization is related to potassic alteration (±magnetite; Sherlock et al., 2012, 2013). The main ore minerals include chalcopyrite, bornite, and molybdenite. Gold mineralization is sub-microscopic, and Laird (2017) suggested it is held in magnetite, chalcopyrite, or bornite. Vandekerkhove et al. (2014) noted that native gold can occur in vein alteration halos at Three Firs. Younger Chilcotin Group (Miocene) olivine-phyric basalts and Kamloops Group (Eocene) volcanic and sedimentary rocks unconformably overlie these older prospective rocks. In airborne magnetic data, Deerhorn, Megabuck, and Takom show magnetic highs; Southeast zone is within a magnetic low (Sherlock et al., 2012, 2013).

3.1.3. Guichon Creek batholith

The Guichon Creek batholith (Late Triassic to Early Jurassic) is a concentrically zoned intrusive body with mafic phases at its margins and younger felsic phases in its interior (Fig. 3; Byrne et al., 2013; D'Angelo et al., 2017). Felsic phases host the Highland Valley deposits, including four producing and past producing calc-alkaline porphyry Cu-Mo deposits (Valley, Lornex, Bethlehem, Highmont), and numerous additional porphyry (and related) mineral occurrences. Each of these deposits is hydrothermally altered, with potassic and phyllic alteration associated with sulphides. Mineralization consists of chalcopyrite, bornite, and molybdenite along faults, as vein fills, in facture haloes, and as breccia infills (Byrne et al., 2013). Magnetite locally occurs with, or near, copper mineralization, but as a whole, the Highland Valley district is within a regional-scale airborne magnetic low (Lesage et al., 2019). The Guichon Creek batholith intruded into Nicola Group (Late Triassic) sedimentary and volcanic country rock (Byrne et al., 2013; Graden, 2013). Ashcroft Formation (Jurassic) siliciclastic rocks and Kamloops Group (Eocene) volcanic rocks overlie the batholith towards the north, and the Spences Bridge Group (Cretaceous) andesites to dacites overlie it towards the southwest (D'Angelo et al., 2017).

3.2. Quaternary geology and ice-flow history

Central British Columbia was repeatedly affected by the Cordilleran ice sheet, with the last glacial cycle spanning from ~30 to 10 ka (Clague and Ward, 2011). This glaciation deposited significant amounts of sediments on the surface of the Interior Plateau, obscuring bedrock. Sediments eroded and deposited beneath the advancing and retreating ice sheet are the focus of drift prospecting studies and are typically defined as till blankets, till veneers, and streamlined tills (e.g., Ferbey et al., 2016b; defined by Deblonde et al., 2019). Other till varieties, such as ridged or hummocky tills, are more likely to consist of supraglacial or englacial sediments (McClenaghan et al., 2013). These tills are typically more reworked and less representative of up-ice bedrock geology than subglacial tills (McClenaghan and Paulen, 2017).

3.2.1. Mount Polley mine and Woodjam prospect areas

The Mount Polley and Woodjam areas are on the eastern boundary of the Fraser Plateau, an area of rolling topography that rises to the east, transitioning into the Quesnel Highlands and the steeper Cariboo Mountains (Holland, 1976). Mainly till blankets (>2 m thick) and streamlined tills from the last glaciation cover the plateau surface and valley sides (Fig. 4). The till thins toward topographic highs where veneers (<2 m thick) cover hilltops with locally exposed bedrock. Less than 5% of the area is bedrock outcrop (Hashmi et al., 2015a; Ferbey et al., 2016a) necessitating exploration by drift prospecting. Subglacial tills in the area are generally highly compact, with a silty sand matrix and 10 to 20 % pebble to boulder clasts (Hashmi, 2015; Hashmi et al., 2015b). The geochemistry and mineral assemblage of tills down ice of Mount Polley reflect the deposit's mineralization and alteration halo for up to 10 km (Hashmi et al., 2015b). The thickness and areal extent of organic

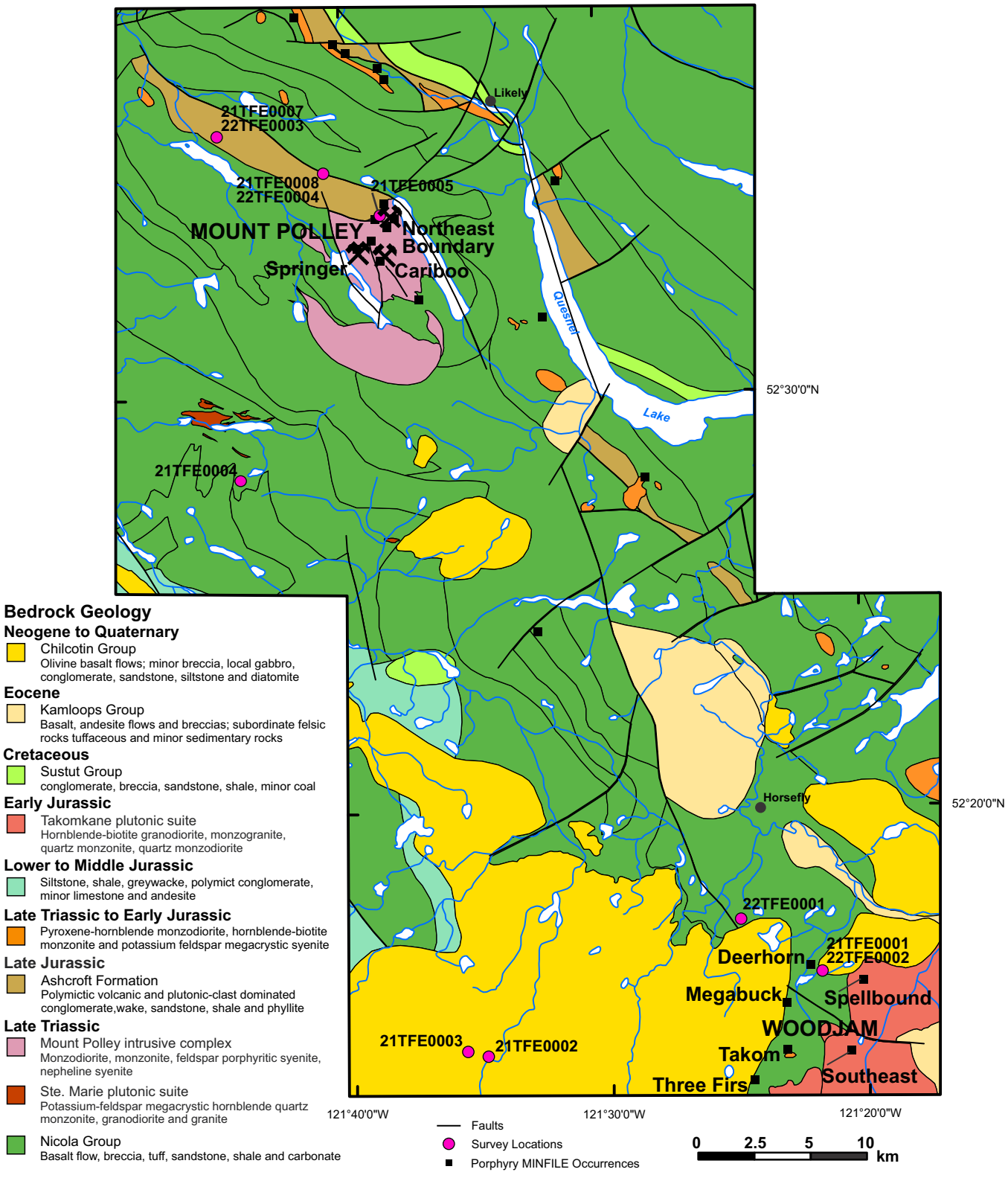

Fig. 2. Bedrock geology of the Mount Polley and Woodjam study areas. Pink points show RPAS survey sites, which are labelled with field station numbers; multiple field station numbers indicate sites where surveys were flown twice in separate field seasons. Bedrock geology modified from Logan et al. (2010), MINFILE occurrences modified from British Columbia Geological Survey (2022).

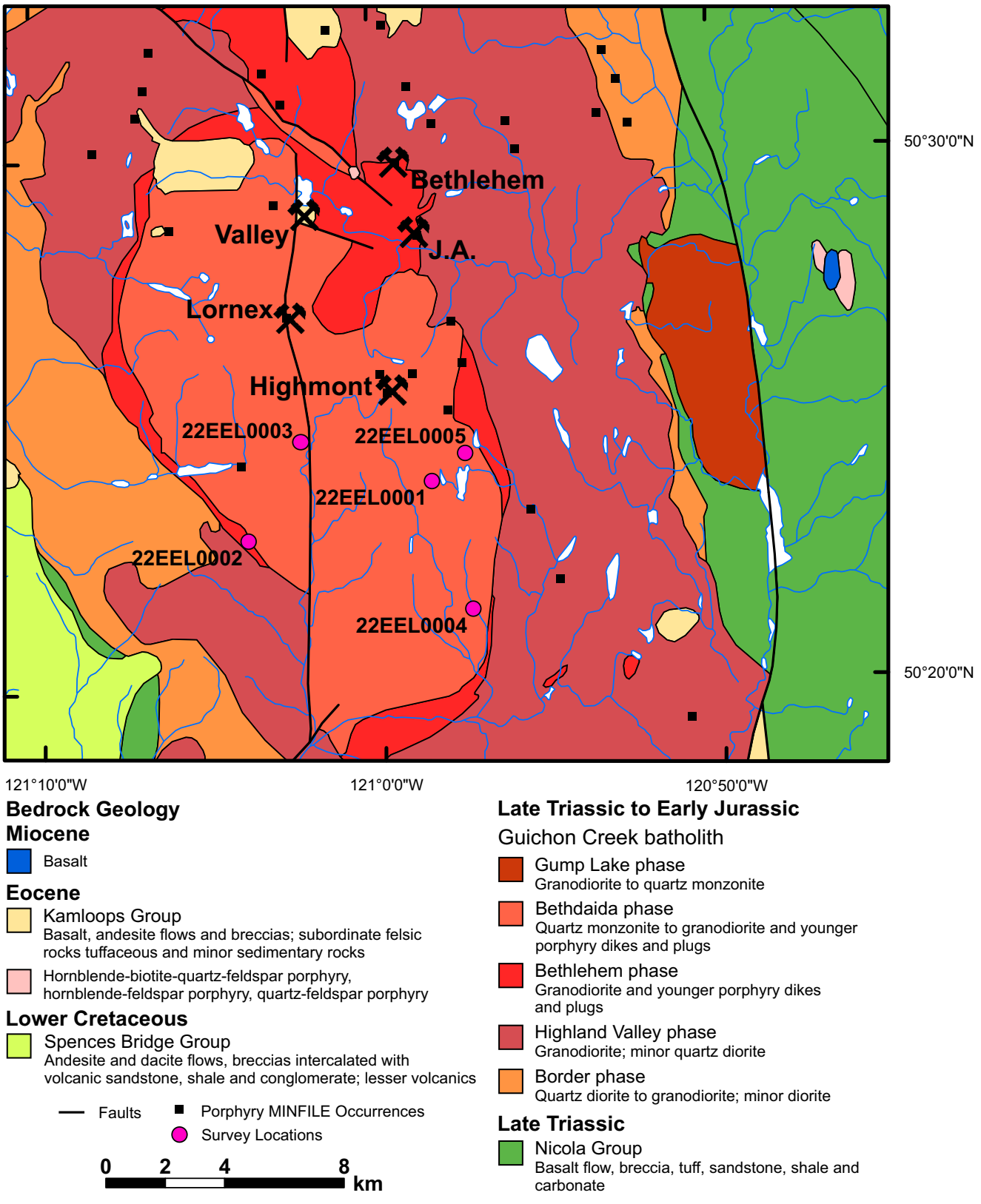

Fig. 3. Bedrock geology of the Guichon Creek batholith study area. Pink points show RPAS survey sites, which are labelled with field station numbers. Bedrock geology from Schiarizza and Church (1996), MINFILE occurrences modified from British Columbia Geological Survey (2022).

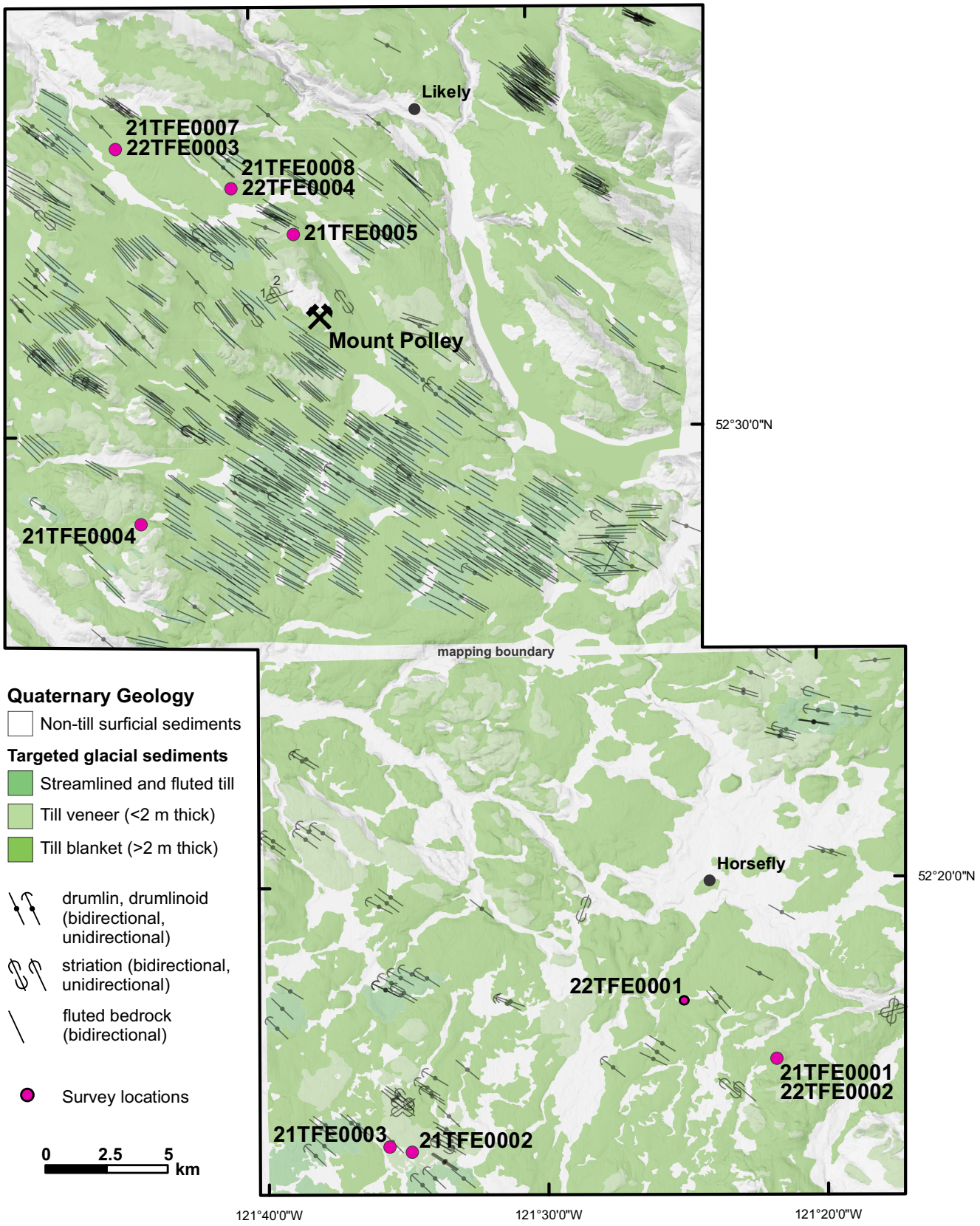

Fig. 4. Regional ice-flow and targeted glacial sediments for the Mount Polley and Woodjam study areas. Ice-flow measurements are modified from Arnold et al. (2021). Glacial sediments are modified from Hashmi et al. (2015a) and Ferbey et al. (2016a).

soil horizons mantling these surficial geology units are variable depending on topographic position, soil moisture, and a source for vegetation accumulation. Glacially streamlined landforms (crag-and-tail ridges, drumlins, flutings) and outcrop-scale indicators (striations, rat tails) show that net glacial transport and predominant ice-flow was to the northwest (Fig. 4; Hashmi et al., 2015a; Ferbey et al., 2016a).

3.2.2. Guichon Creek batholith

The Guichon Creek batholith area is within the Thompson Plateau, an area of gently rolling hills and low relief (Holland, 1976). Tills account for most of the surficial sediments covering the Guichon Creek batholith (Fig. 5) and can be divided into two main facies: ablation and subglacial. Ablation tills are poorly compacted, have up to 35% clasts, a coarse silty sandy matrix (63% sand, 34% silt, 2% clay) and commonly have a slightly undulating to hummocky surface expression (Ferbey et al., 2016b). Based on a low consolidation, large median clast size, and surface expression, Ferbey et al. (2016b) interpreted these tills as being deposited by melting ice. The subglacial facies typically has fewer clasts (15%), a higher proportion of faceted and striated clasts (20% of total clasts), a siltier matrix (51% sand, 43 silt, 6% clay), and is well compacted. (Ferbey et al., 2016b). Subglacial tills are commonly veneers, blankets, or streamlined and typically have clasts of a single lithology, usually felsic intrusive rock from the Guichon Creek batholith suggesting minimal transport. Bedrock outcrops appear throughout the till map units, most commonly in veneer and streamlined till landforms. Organic soil horizons mantling till units are thinner than those in the Mount Polley and Woodjam areas and were drier when we collected our data. In contrast to the Mount Polley and Woodjam areas, ice flow through the Guichon Creek batholith area was toward the south-southeast during the last glacial maximum, as demonstrated by streamlined glacial landforms and outcrop-scale erosional features (Fig. 5; Ferbey et al., 2016).

4. Methods

We flew gamma-ray spectrometer, magnetometer, lidar, and aerial photographic surveys at the Mount Polley mine, Woodjam prospect, and Guichon Creek batholith areas (Figs. 1, 6). As part of the validation process, we also made ground magnetic susceptibility and radiometric measurements and collected new till samples; these data and the validation of results will be considered in forthcoming publications.

4.1. RPAS flight regulations

RPAS licencing, registration, and regulation are set by Transport Canada. All pilots flying aircraft weighing more than 249 g must pass a standardized exam to become licenced, and their aircraft must be registered (Transport Canada, 2022). Additionally, pilots can only fly an RPAS up to 122 m above ground, and the aircraft must be within the pilot's visual line of sight at all times, a factor that influenced our site selection.

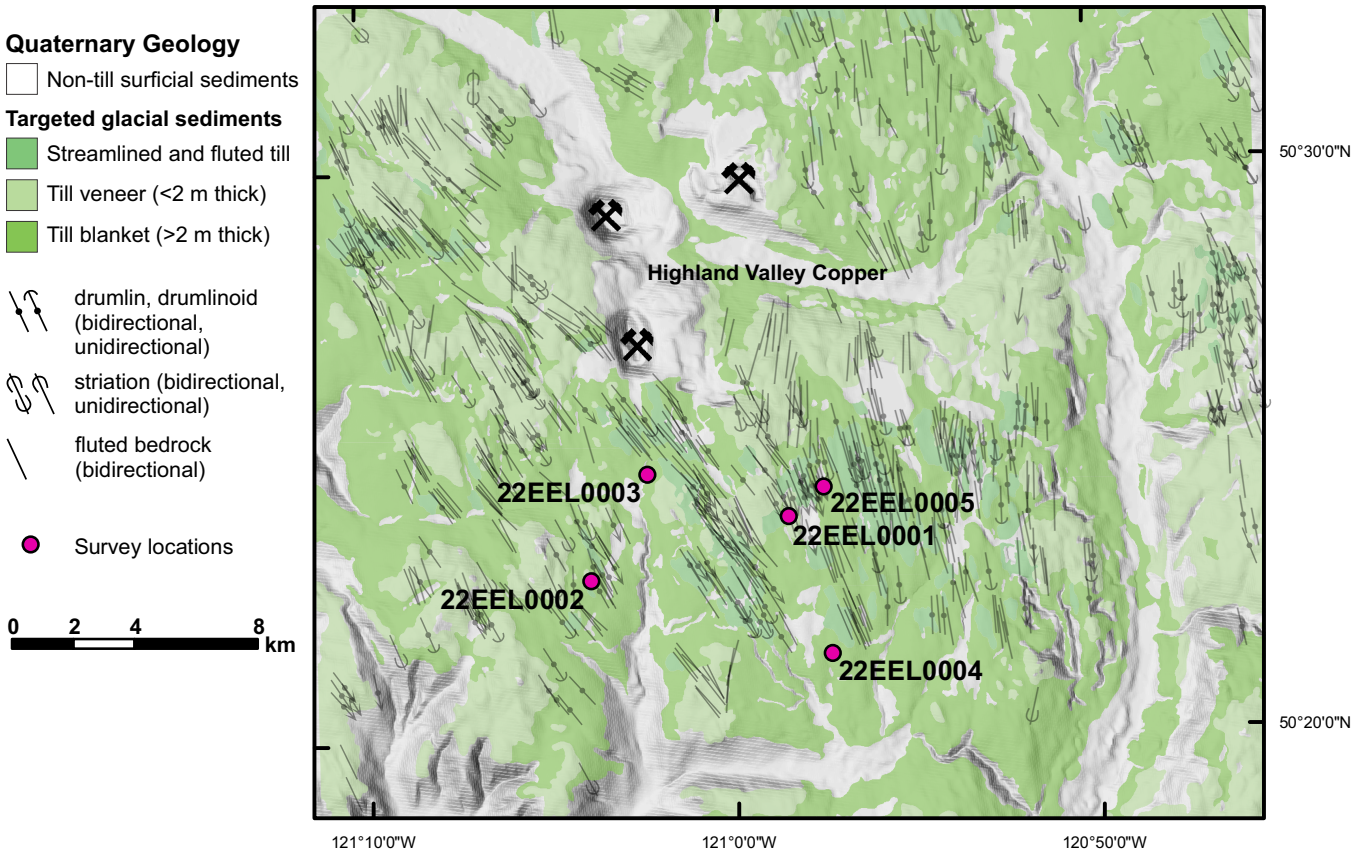

Fig. 5. Regional ice-flow and targeted glacial sediments for the Guichon Creek batholith study area. Ice-flow measurements are modified from Arnold et al. (2021). Glacial sediments are modified from Plouffe and Ferbey (2018).

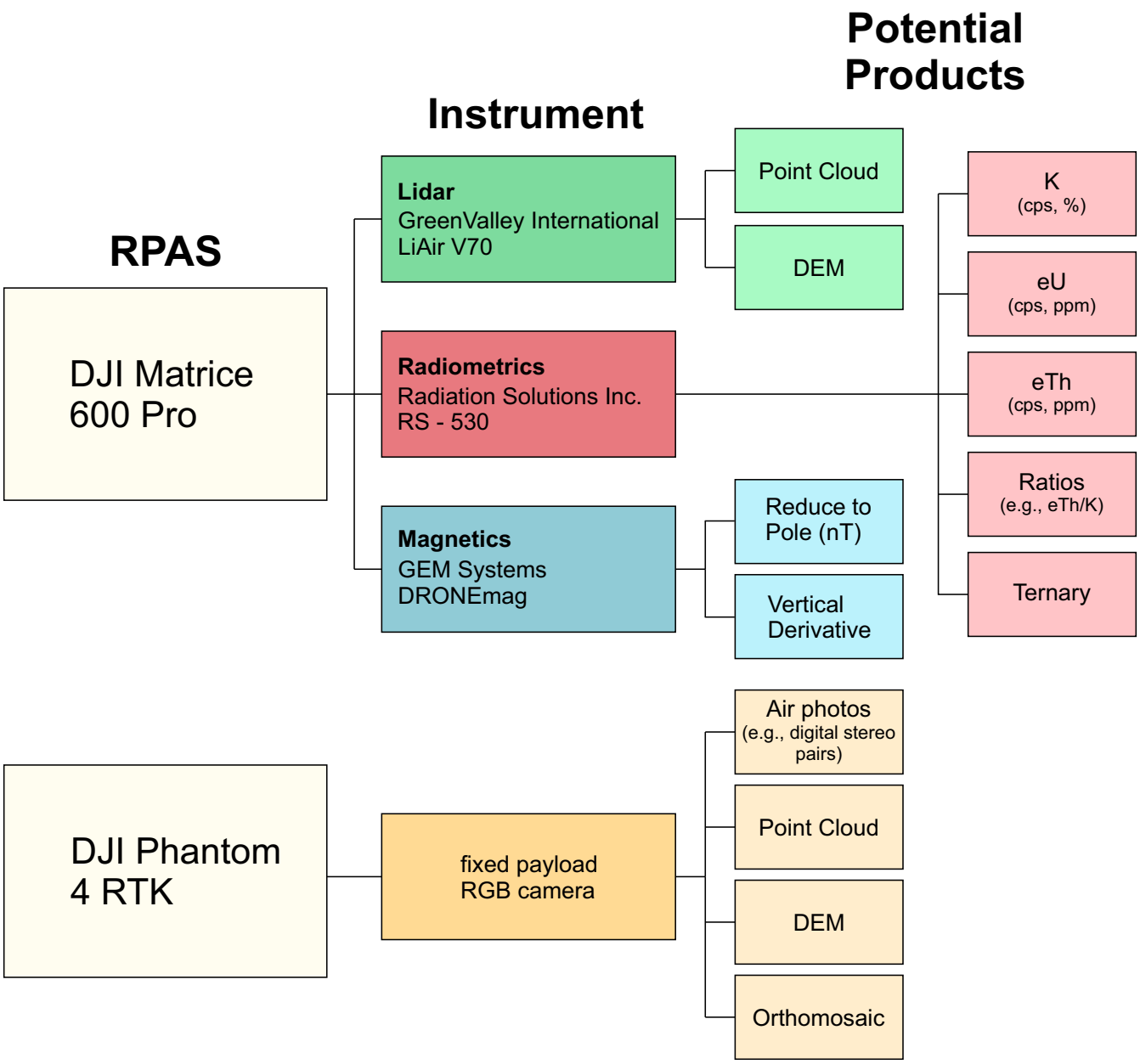

Fig. 6. Collection methods and products generated at each RPAS survey area. Instrument boxes show the instrument used to acquire the data corresponding to their RPAS platform. Potential products are coloured corresponding to the sensor that was used for collection.

4.2. Survey area selection

The primary criteria we used to select a survey area was that it had to be underlain by a subglacial till derived from a known porphyry source, as determined by existing bedrock and surficial geology maps (Hashmi et al., 2015a; Ferbey et al., 2016a; Plouffe and Ferbey, 2018; Logan et al., 2010; Schiarizza and Church, 1996). It was also important that the area have forestry cutblocks that would let us maintain visual line of sight during flight and allow the aircraft to fly low and ultra-low altitude terrain-following surveys < 15 m above ground level. We used recent 10 m resolution Sentinel-2 satellite imagery to assess the spatial distribution and age of cutblocks relative to areas with ideal geology. In the field, we assessed cutblock flyability and made final decisions on survey placement based on these observations.

4.3. RPAS aircraft

4.3.1. DJI Matrice 600 Pro (M600)

We used a DJI Matrice 600 Pro (M600) RPAS to fly magnetic, radiometric, and lidar sensors (Figs. 7-9). The M600 is a commercially available hexacopter with a payload capacity of 6 kg. On the underside of the aircraft are two mounting rails, an 18 V DC port for powering external payloads, and landing gear that can be retracted to avoid sensor obstruction. Six electric motors are each powered by their own battery. This adds power redundancy to the aircraft as it is still flyable using five

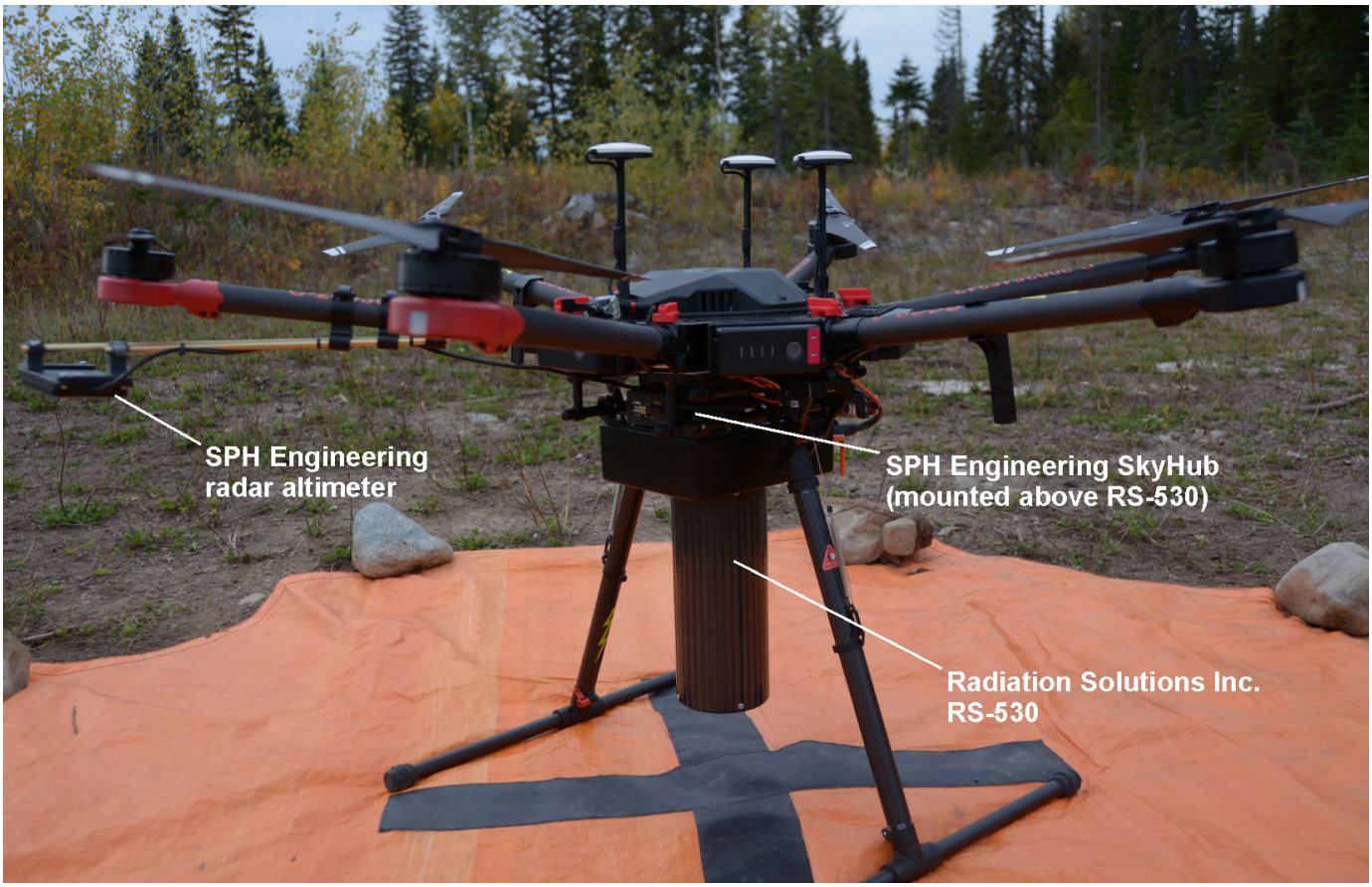

Fig. 7. DJI Matrice 600 Pro (M600) RPAS used to acquire lidar, magnetic, and radiometric data. A Radiations Solutions Inc. (RSI) RS-530 gamma-ray spectrometer is mounted beneath, above which is an SPH Engineering Skyhub onboard computer. An SPH Engineering radar altimeter (NRA24) is mounted on an arm.

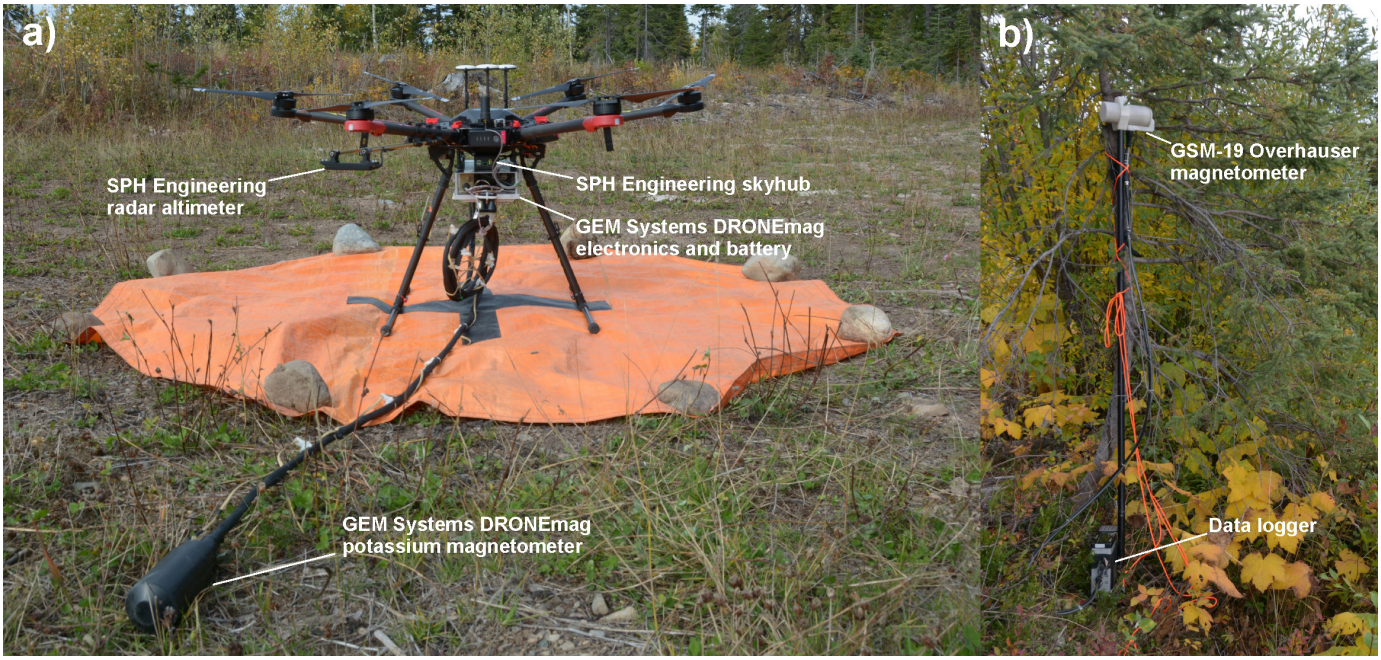

Fig. 8. RPAS magnetometer acquisition equipment. **a)** GEM Systems GSMP-35 U DRONEmag potassium magnetometer mounted on a DJI Matrice 600 Pro. The instrument's electronics and battery are housed in a custom tray mount. The magnetometer sensor is slung 2.5 m from the mount's base. **b)** GSM-19 Overhauser magnetometer attached to a tree; data logger at base.

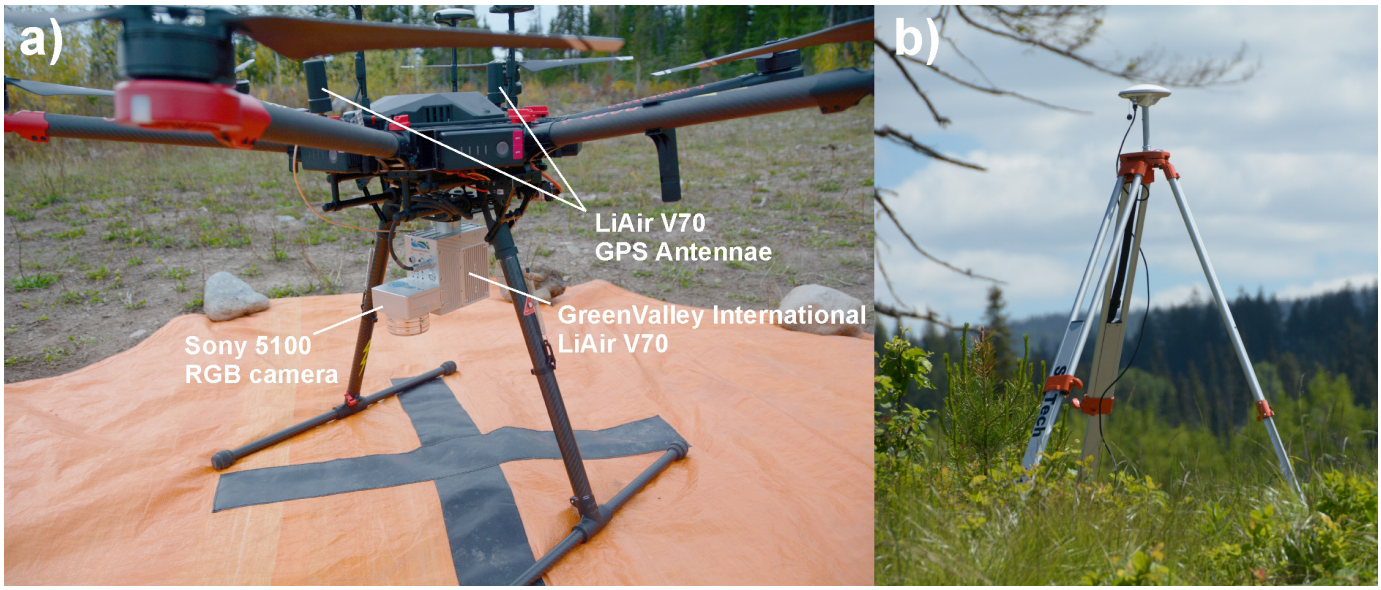

Fig. 9. Lidar acquisition equipment. **a)** Green Valley LiAir V70 mounted on a DJI Matrice 600 Pro aircraft with two external global navigation satellite system antennae mounted at the top. The Sony 5100 RGB camera module is indicated with the RGB camera lens directly below. **b)** LiAir V70 global navigation satellite system base station.

motors. The M600 uses three global navigation satellite system (GNSS) antennas to accurately maintain azimuth headings and determine x, y, and z positions.

The M600 aircraft does not have obstacle avoidance systems commonly seen in modern consumer RPAS. To increase safety, a custom first-person view (FPV) camera was mounted to the front of the RPAS. The FPV camera feed is viewable in real time on an android display allowing pilots to estimate aircraft height and manually avoid obstacles when designing a survey. We also used a laser range finder to determine obstacle heights (e.g., trees along cutblock edge, snags in cutblock) so they could be accounted for during survey design. Obstacle locations in a survey area were mapped using coordinates from visiting obstructions with a handheld GPS or flying over them with the aircraft. We then used these coordinates to manually delineate a 'safe zone' for flying each low-altitude survey.

We used SPH Engineering's Universal Ground Control Software (UgCS) flight planning package to design, upload, and fly autopilot surveys (UgCS, 2023). UgCS provides flight customization options not available in DJI's proprietary flight planning software, DJI GO. Additionally, the UgCS has a terrain-following functionality which uses a high-resolution DEM or active laser or radar altimeter to maintain a constant survey height above the ground. To enable terrain following, we chose to use SPH Engineering's Nanoradar NRA24, a small K-Band radar altimeter that is mounted on a front arm of the aircraft (Fig. 7). The radar altimeter communicates in real time with the M600 aircraft through SPH's Skyhub onboard flight controller, passing on instructions to increase or decrease altitude to maintain a pre-set altitude above ground (approximately ±50 cm depending on vegetation) when flying an autopilot survey. This feed from the radar altimeter is transmitted to UgCS running on a laptop.

Terrain following can prevent RPAS crashes during low altitude (5-30 m above ground level) and ultra-low altitude (16 cm – 5 m above ground level) surveys in variable topography with obstructions by ensuring the aircraft maintains a minimum (safe) vertical distance between the ground or obstructions (large boulders, logs, shrubs, and small trees). Maintaining a constant altitude above ground is also important for some sensors (e.g., gamma-ray spectrometer and magnetometer) because it ensures that data variation is related to geology and not changes in distance between the geophysical sensor and the ground. In other instances (e.g., lidar, magnetometer, and gamma-ray spectrometer), terrain following helps to maintain consistent resolutions and ensure the sensors capture data over the same sized area (i.e., swath width) throughout a survey.

4.3.2. DJI Phantom 4 RTK (P4RTK)

A DJI Phantom 4 RTK (P4RTK) was used to collect air photos for surficial geology mapping and three-dimensional modelling. The P4RTK has a fixed mechanical shutter RGB camera with a 20-megapixel, 1-inch CMOS sensor (Fig. 10). The camera is mounted to a stabilized three-axis gimbal allowing it to pan and tilt during flight. The aircraft is a quadcopter and uses a single battery to fly autopilot missions designed for photogrammetry applications. The P4RTK has features that enable the capture of images with highly accurate spatial locations including: an RTK module and base station, purpose-built flight planning software for photogrammetry-specific missions, and DJI's TimeSync system (DJI, 2020, 2022).

4. 4. Radiometric, magnetic, lidar, and aerial photography survey instrumentation

4.4.1. Radiometric

A Radiation Solutions Inc. (RSI) RS-530 gamma-ray spectrometer was used to collect radiometric data (Fig. 7); Table 1). The sensor uses a single 3" x 3", thallium-doped, sodium iodide (NaI(TI)) crystal scintillator, housed in a vertical carbon fibre tube. Compared to a bismuth germanium oxide (BGO) scintillator, NaI(Tl) produces a higher light output, resulting in increased sensitivity and a faster collection rate (McGregor,

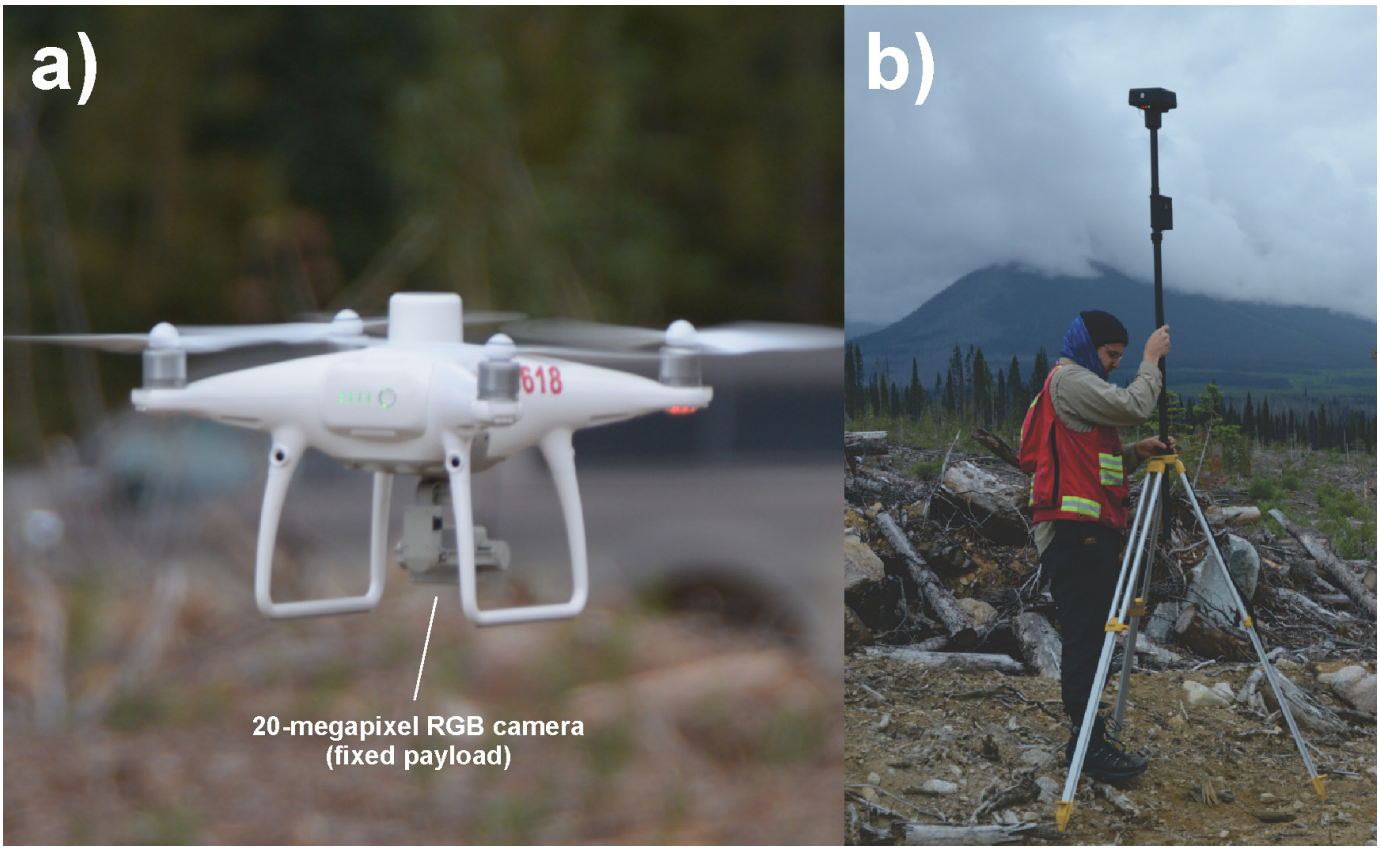

Fig. 10. DJI Phantom 4 RTK (P4RTK) RPAS used to acquire air photographs in this study. **a)** Aircraft in flight with the camera facing away from the viewer. **b)** Mobile base station being set up.

2018). The instrument weighs 3 kg, mounts directly to the bottom of the M600 aircraft, and is powered by the aircraft's 18 V DC port. The instrument has a fixed sample rate of 1 Hz and collects data across the 12 keV to 3 MeV energy range. The RS-530 integrates with RadAssist, Radiation Solutions Inc's propriety software, to visualize data in real time during collection. RadAssist also can process and correct data after the completion of a survey.

4.4.2. Magnetic

A GEM Systems DRONEmag (GSMP-35U) magnetometer was used to collect magnetic data (Fig. 8; Table 2; GEM Systems, 2023a). The instrument weighs 2.0 kg and includes an optically pumped potassium sensor, battery, laser altimeter, data logger, global navigation satellite system (GNSS) antenna, inertial measurement unit (IMU), and 5 m cable to transfer data between the slung sensor and aircraft-mounted data logger. We built a custom aluminum tray mount to house the magnetometer components, which attaches to the M600 aircraft mounting rails. The laser altimeter was fixed to the front of the tray mount, ensuring it had an unobstructed view of the ground surface, and the global navigation satellite system antenna was mounted to the top of the aircraft for an unobstructed view of the sky. The sensor was slung 2.5 m below the RPAS, out of range of electromagnetic noise from the RPAS motors and electronics, and the unused cable was coiled and attached to the underside of the tray mount. The system we used did not allow for real-time transmission of data during a survey. This feature is available with additional hardware.

A GSM-19 Overhauser base station was used to collect magnetic readings while RPAS surveys were conducted (Fig. 8; GEM Systems, 2023b). The base station collected data at 5 Hz (one measurement every 0.2 s) with a resolution of 0.01 nT. Data from both the RPAS and base station magnetometers were uploaded to a laptop using GEM System's GEMLink software. This software was also used to initialize and set up the DRONEmag before flying a survey.

4.4.3. Lidar

A GreenValley International LiAir V70 was used to collect lidar data (Fig. 9). The instrument attaches to the M600 mounting rails and is powered using the aircraft's 18 V DC power port. The LiAir V70 is a 1.1 kg, Livox AVIA sensor instrument with a 70.4° field of view. A Sony A5100 mechanical shutter, 24.3 MP camera with an APS-C type CMOS sensor is integrated into the lidar instrument housing and collects RGB photos to create colourized point clouds. The instrument uses two global navigation satellite system antennas, which are mounted on the top of the aircraft for an unobstructed view of the sky. The sensor has a scan rate of 240,000 pts/s (first returns) and a detection range of 450 m at 80% reflectance (Table 3). During surveys with the LiAir V70, a global navigation satellite system base station records data used for an automatic post-processing spatial correction.

Table 1. Technical parameters of the Radiation Solutions Inc. RS-530 gamma-ray spectrometer.

Parameter	Aircraft, instrument, and survey specifications
Aircraft platform	DJI Matrice 600 Pro
Instrument	Radiation Solutions Inc. RS-530 gamma-ray spectrometer
Sensor type	3” x 3” NaI (Tl) crystal
Instrument weight	3.0 kg
Flight time	approximately 20 min
Instrument size	20 x 15 x 35 cm
Flying height	5 to 10 m above ground
Flying speed	1 to 2 m/s
Product types	total count, radioelement counts, K (%), eU (ppm), eTh (ppm) concentrations
Energy range	12keV to 3MeV
Sample rate	1 Hz (one measurement per second)
Spatial resolution*	1.67 to 3.33 m/pixel*

*Spatial resolution of gridded representations is manually set as a factor (1:3) of line spacing. Decreasing line spacing yields a finer spatial resolution.

Table 2. Technical parameters of the GEM Systems DRONEmag GSMP-3U magnetometer.

Parameter	Aircraft, instrument, and survey specifications
Aircraft platform	DJI Matrice 600 Pro
Instrument	GEM System DRONEmag
Sensor type	Optically Pumped Potassium Sensor
Instrument size	Approximately 30 x 15 x 10 cm with sensor slung 2.5 m below RPAS
Instrument weight	2.0 kg
Flight time	approximately 20 minutes
Flying height	5 to 10 m above ground
Flying speed	2 m/s
Product types	total field (nT), 1st vertical derivative, high pass
Instrument sensitivity	0.0002 nT at 1 Hz
Instrument resolution	0.0001 nT
Dynamic range	15,000 to 120,000 nT
Sample rate used	10 Hz (one measurement every 0.1 sec)
Spatial resolution*	1.67 to 3.33 m/pixel*

*Spatial resolution of gridded representations is manually set as a factor (1:3) of line spacing. Decreasing line spacing yields a finer spatial resolution.

Table 3. Technical parameters of the Green Valley LiAir V70 lidar sensor.

Parameter	Aircraft, instrument, and survey specifications
Aircraft platform	DJI Matrice 600 Pro
Instrument	GreenValley International LiAir V70
Sensor Type	70.4-degree field of view, Livox AVIA lidar sensor with 24.3 MP, mechanical shutter, camera
Instrument size	17.8 x 8.2 x 14.0 cm
Instrument weight	1.1 kg
Flying height	80 to 100 m above ground
Flying speed	4 m/s
Products	Colourized point cloud, digital elevation model
Scan rate	240,000 pts/s (first returns)
Spatial resolution*	25 cm/pixel*

*Resolution is based on a range of parameters and constraints including flying height, speed, overlaps, computer hardware, and desired processing time.

Table 4. Technical specifications of the DJI Phantom 4 Pro RTK aircraft and photogrammetry products.

Parameter	Aircraft, instrument, and survey specifications
Aircraft platform	Phantom 4 RTK
Sensor type	20 MP, mechanical shutter, RGB camera
Flying height	80 to 100 m above ground
Flying speed	4 m/s
Product types	point clouds, orthomosaics, digital elevation models
Sidelap	70 %
Endlap	80 %
Spatial resolution*	~ 10 cm/pixel (DEM) ~ 2 cm/pixel (orthomosaic)

*Resolution is based on a range of parameters and constraints including flying height, speed, overlaps, computer hardware, and desired processing time.

Two figures of eight were flown after taking off, and before landing, to calibrate the lidar instrument. The LiAir V70 has a stated system accuracy of ±5 cm (Green Valley International, 2017) and was not assessed as part of this project.

4.4.4. Aerial photography

With a fixed RGB camera, the DJI Phantom 4 RTK (P4RTK) aircraft uses a real-time kinematic (RTK) base station to calculate spatial correction information that is used to accurately fly autopilot surveys and record x, y, and z positions for each photograph taken (Fig. 10; Table 4). These photo locations have an overall accuracy of 1 cm horizontally and 1.5 cm vertically (DJI, 2020). For our application, this increased spatial accuracy allows surveys to be flown without ground control points thereby decreasing the time required for collection and post-processing (Elia and Ferbey, 2019).

4.5. Survey design, data acquisition, and data processing

4.5.1. Radiometrics

Radiometric surveys were flown with 5 to 10 m line spacing at 5 to 10 m above ground level using active terrain following (Fig. 11). Radiometric surveys began after 10:00 AM local time or 12 hours after the end of a ground-soaking rainfall, to minimize radon interference with uranium counts and to minimize the attenuation of total counts due to increased soil moisture (such as described by Amestoy et al., 2021). The RS-530 gamma-ray spectrometer communicates with a laptop running RadAssist over a Wi-Fi or ethernet connection to initialize and set up the spectrometer and start recording data before a survey was flown. After flying a survey, RadAssist was used to download, correct, and check the positional accuracy of the data before the instrument was turned off and disassembled. Data were downloaded directly from the instrument using a USB memory stick.

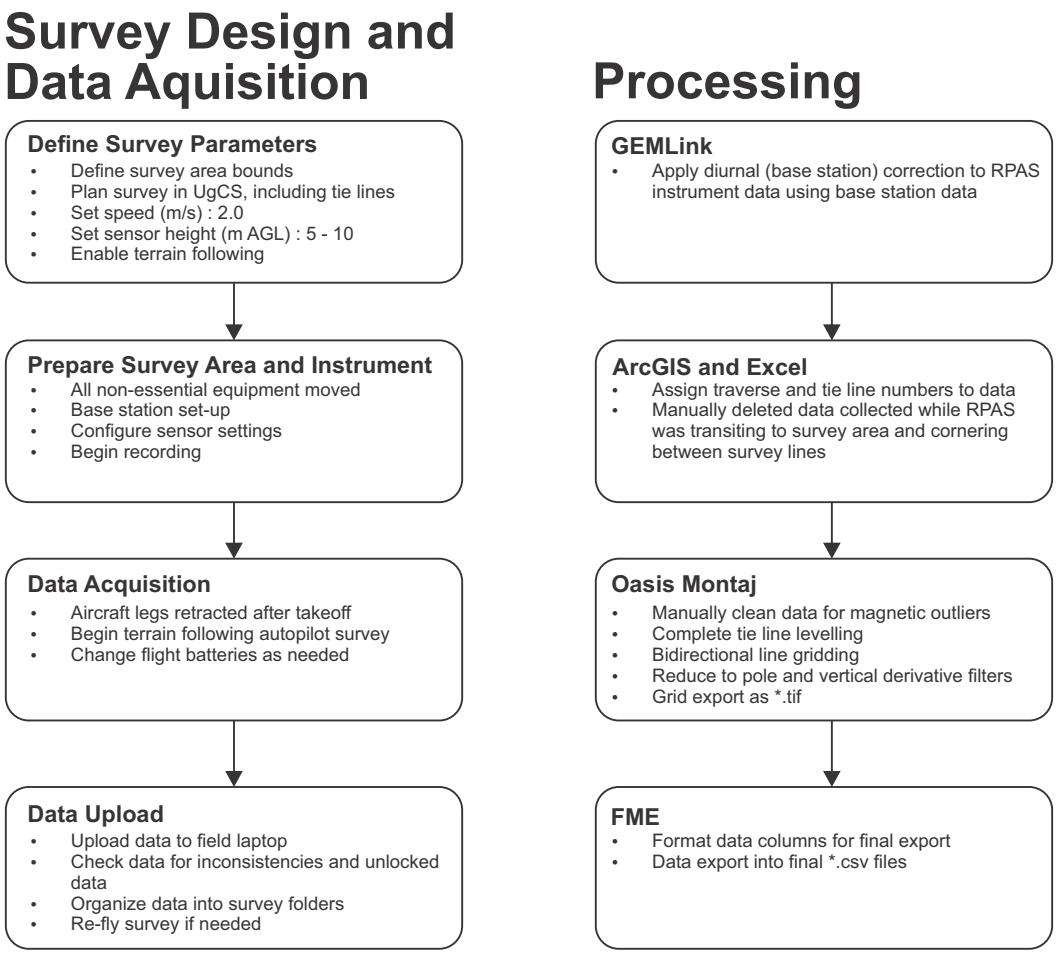

Fig. 11. Flight and processing workflow for generation of magnetic grids and data.

Radiometric data were processed in RadAssist, ArcGIS, Excel, and Oasis Montaj. We used RadAssist to select data collected over each survey area, removing points where the aircraft was on the ground or transiting to and from an autopilot survey. Once a rough collection of survey data was assembled, we exported a preliminary nine-component noise adjusted singular value decomposition (NASVD)-filtered dataset and analyzed the results in Excel. For our data, we found the first five or six components adequately described the radiometric dataset, the higher order ones only containing noise; data were then processed using these component values.

The instrument was pre-calibrated by Radiation Solutions Inc. to determine stripping ratios and sensitivities (Tables 5, 6) These correction factors are specific to each spectrometer. Stripping ratios remove the effects of Compton scattering within the gamma-ray spectrum, whereby a proportion of counts measured in the thorium window affect the uranium and potassium window counts, and some of the counts measured in the uranium window affect the potassium window counts. After corrections for stripping, sensitivities convert the corrected count to concentrations of K (%), eU (ppm) and eTh (ppm). To better understand the attenuation of K, eU (using the ^{214}Bi element) and eTh (using ^{208}Tl) count rates in air, we collected data while hovering the sensor at increasing heights above the ground surface. These data were plotted and fitted with a line to determine an altitude beta factor (post-processing correction factor) accounting for K, eU and eTh attenuation in the layer of air between the surface of the Earth and the detector. We determined a K value of 0.011 for 2022 and 0.035 for 2021. Radiation Solutions Inc.'s altitude beta determinations for eU and eTh of 0.00828 and 0.00783 were used for data in both years. The height correction was applied using the altitude beta factor and the fixed elevation from the radar altimeter (m above ground level). These factors were input into RadAssist and a final data export was completed, which included stripped, NASVD, and height-corrected counts and concentrations.

Exported data were brought into Excel to clean data headings and reduce the number of columns, and then into ArcGIS to assign line numbers and remove data collected while the instrument was cornering and transiting between flight lines. In 2022, we switched from a small global navigation satellite system antenna mounted on the RS-530 instrument below the aircraft to one mounted to the top of the aircraft. Data from both years required additional spatial correction to ensure data points plotted correctly; both corrected and uncorrected positional data are included in the accompanying data tables (radiometric folder in <BCGS_GF2023-07.zip>).

Table 5. Calibration parameters for data conversion and export of gamma-ray spectrometer data from RadAssist. Cosmic values account for radiation from space, unrelated to the measured source on Earth. Altitude betas correct for attenuation of gamma-rays in the air between the sensor and source. The sensor coefficients (sensitivities) convert counts to concentrations for each energy window. The start and end channels define energy windows in RadAssist channel-8 (0.024 MeV), 457 (1.371 MeV), 523 (1.569 MeV), 553 (1.659 MeV), 620 (1.860 MeV), 803 (2.409 MeV), 937 (2.811 MeV). These values were used as inputs for RadAssist where corrections and conversions were automatically applied on export.

ROI	Name	Start Channel	End Channel	Cosmic	Altitude Beta	Sensor Coefficient
01	TotCount	8	937	0	0.00782	1
02	Potassium	457	523	0.09068	0.011/0.035	3.81792
03	Uranium	553	620	0.04981	0.00828	0.33207
04	Thorium	803	937	0.03704	0.00783	0.13885

Table 6. Calibration coefficients matrix from RadAssist. This table shows the coefficients, or stripping ratios, used to reduce interference and account for Compton scattering between energy windows for each radioelement into the other. These values were used as inputs for RadAssist where stripping ratios were automatically applied on export.

	TotCount	Potassium	Uranium	Thorium
TotCount	1	0	0	0
Potassium	0	1	0.942	0.649
Uranium	0	0	1	0.474
Thorium	0	0	0.042	1

Oasis Montaj was used to produce K, eTh, and eU, as well as eTh/K, eU/eTh, and eU/K ratio grids from these corrected data. In each case, we used minimum curvature interpolation with a cell size of one-third line spacing. Variation caused by soil moisture or vegetation creates gridded data that emphasizes these differences and may not show geological changes. In these cases, a low-pass de-sampling factor of 2 or 3 may be applied to the grid to reduce large-scale variation and show smaller-scale geological differences. In some instances, particularly over small survey areas, the minimum curvature function produces grids that extend far beyond the RPAS survey boundaries. In this case, we instead used an inverse distance weighting (IDW) algorithm that extrapolates a shorter distance from the measured data points compared to minimum curvature.

4.5.2. Magnetics

Magnetics surveys were flown with 5 to 10 m line spacing at 5 to 10 m above ground level (Fig. 12). One exception to these parameters was collected over Deerhorn mineralized zone (21TFE0002_2) with 100 m line spacing at 97.5 m above ground level following a coarse DEM. Before conducting a magnetics survey, all non-essential ferrous equipment (e.g., truck) and sources of electromagnetic noise (e.g., gas-powered AC generator) were moved outside the survey area to minimize magnetic interference. The base station magnetometer was also set up just outside the survey area to record total field magnetics at 5 Hz during each survey.

The DRONEmag was set up, using GEMlink, with a datum of 56,000 nT and a sampling rate of 10 Hz. The sensor has a large dynamic range (15,000 to 120,000 nT) and so the sampling range was reduced to decrease the amount of time the sensor spent searching for a signal. The aircraft was launched and landed manually, and survey grids were flown on autopilot with active terrain-following enabled. Tie lines were placed perpendicular to traverse lines, with about one tie line for every three traverse lines.

Data were downloaded from the instrument immediately after each survey so that a preliminary assessment of data quality could be completed. In ArcMap, the ‘locked’ and ‘unlocked’ status of each measurement was assessed to ensure we collected an adequate amount of data for gridding. The instrument becomes unlocked when the centreline of the sensor exceeds an angular threshold relative to the inclination of the local magnetic field, and an erroneous value will be recorded. Unlocking typically occurs during acceleration at the beginning of flight lines, during cornering between flight lines, and over abrupt changes in topography when aircraft altitude adjustments cause the slung magnetometer to swing. Data points were deleted where instrument unlocking occurred, creating data gaps along the traverse and tie lines. This was a problem during the 2021 field season but was partially dealt with by re-flying the gridded survey, sometimes in the opposite direction. In 2022, we experimented with sensor alignment relative to the inclination of the local magnetic field, which reduced the number of ‘unlocked’ data points.

Diurnal corrections were performed in Oasis Montaj (2021 data) and GEMlink (2022 data). Because the base station and RPAS instrument collected data at different rates, an interpolated base station value was applied to every second RPAS measurement. Using ArcGIS, data were separated into individual traverse and tie lines. Removal of outlier points, tie line levelling, and reduction to pole filtration were then completed in Oasis Montaj. The traverse line data were then gridded using bidirectional line gridding with a cell size of one-third line spacing. We further filtered the reduced-to-pole data using a first vertical derivative filter.

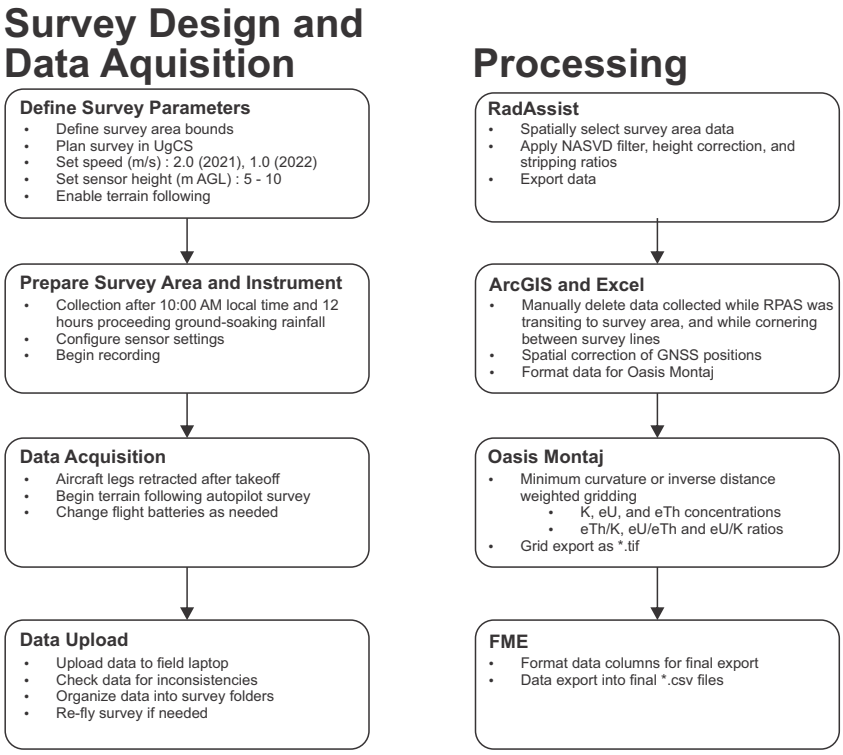

Fig. 12. Flight and processing workflow for generation of radiometric grids and data.

4.5.3. Lidar

Lidar surveys were flown at 80 to 100 m above ground level, at 4 to 5 m/s. An Excel spreadsheet (modified from Alsadik and Remondino, 2020) was used to calculate survey height and line spacing to ensure a 50% overlap between scans; active terrain-following was not used for lidar surveys (Table 7). In rare instances, specifically in areas of rising topography, terrain-following was enabled using a course (30 m) shuttle radar topography mission (SRTM) digital elevation model instead of the radar altimeter. This was required because a decreased distance between the sensor and the ground causes the swath size to decrease, which reduces scan overlap and may create holes in the data. Lidar surveys were designed to extend across larger areas than the magnetometer or gamma-ray spectrometer surveys.

Table 7. Example of lidar parameters for a survey flown at 80 m above take-off location.

Inputs	**Value**
Flying height above the ground level (m)	80
Scanning range of the lidar (m)	119.75
Horizontal FOV (degrees)	70.4
Side lap (%)	50
Output	
Along track scanning width (m)	119.75
Across track swath width of the scanning (m)	178.20
Separation distance between the flight lines (m)	89.10

The onboard camera was set to collect photos every 2 seconds once the aircraft was >50 m above the take-off location. For calibration, two figures of eight were flown before and after completing the autopilot survey. Survey time was reduced by hot swapping aircraft batteries. This ensured that power to the lidar instrument was maintained, avoiding time-consuming reinitializing and calibrating. The global navigation satellite system base station was set up within the survey area and collected data for 10 minutes before and after a lidar survey. Data from the base station and lidar instrument were assessed for data quality at the end of each survey.

GreenValley's LiGeoreference software suite was used to first process the raw lidar data following instructions in the LiAir user guide (Green Valley International, 2017). Flight lines were delineated manually; position and orientation system (POS), georeferencing and colourization functions were then performed on them. A boresight correction was used to align individual lidar swaths to their neighbours (rotational corrections of < 1° were always maintained, translation corrections were not required), and outlier points were removed. From here, a point cloud of individual swaths was exported from LiGeoreference and imported into Green Valley's Lidar 360 or Cloud Compare, an open-source software package, to classify ground points (e.g., remove vegetation) and produce bare-Earth DEMs. These software packages calculate ground points using different techniques and, depending on the survey area, can change the number and quality of classified ground points. For example, Cloud Compare uses a Cloth Simulation Feature (CSF), whereas LiDAR360 uses a triangulation technique to classify ground points. In either case, swaths were joined to form a point cloud. The point cloud's ground points were extracted from the dataset using parameters determined on a case-by-case basis

and used to create a DEM; the points representing trees and low brush remained unclassified. An average density of 79 points/m^2 in ground-classified data at one of the Woodjam sites (21TFE0002, Fig. 2) indicates a supported cell size up to 0.25 m (extrapolated values from Table 4 in GeoBC, 2017). Because a goal of the project is to create DEMs for field use rather than publication-quality data, we did not perform ground-control or vertical accuracy assessments.

Data were exported as *.tiff files at multiple resolutions (0.25, 0.5 and 1 m cell size) and hillshade models of these bare-Earth DEMs were produced using the Image Analysis toolbar in ArcMap. An azimuth of 45º and a z-factor of 1 were typically used, and the illumination azimuth varied depending on the orientation of features we wished to highlight within a survey area. We visually assessed each resolution of hillshade models to determine the best product for our application and saved these as *.pdf files. It is important to note that some sections of the DEMs may not support the gridded resolution of the data. However, these products were designed as field and mapping aides, and areas of low-density data can be ignored or treated with less confidence.

4.5.4. Aerial photography

Air photo surveys were flown at 80 to 100 m above the take-off location, at 4 to 5 m/sec. DJI GS RTK software, running on the RPAS controller, was used to plan the surveys. The software automatically designs a survey (including flight line spacing) based on present parameters like survey boundaries, flight speed, and photo overlap. The surveys were flown on autopilot and were designed to cover the same area as the lidar surveys.

We used the procedures outlined by Elia and Ferbey (2019) to acquire and process air photos. This workflow is optimized for surficial geology applications and provides adequate spatial resolution for this project. The resultant photogrammetric DEMs were manipulated in ArcGIS using the same techniques applied to lidar bare-Earth DEMs.

5. Magnetometry and gamma-ray spectrometry data; lidar and air photo products

The <BCGS_GF2023-07.zip> folder accompanying this report contains raw and processed magnetic and gamma-ray spectrometry radiometric data and lidar and air photo products from surveys conducted in the 2021 and 2022 field seasons (Table 8). The raw lidar and aerial photography data files are inordinately large (>5 GB each) and are not provided as part of this release.

The raw magnetic data from the RPAS and base station are provided as *.csv files. Processed magnetic RPAS point data are also provided in *.csv format, and gridded magnetic products are available as *.tiff maps and Geosoft *.grd files. For radiometrics, a single *.csv file contains both uncorrected counts and corrected concentration data. These data are available with both uncorrected and corrected coordinate locations. The final corrected grids are available in *.tiff and *.grd files for each element and ratio. The filename number prefix refers to the year of data collection (21 = summer 2021, 22 = summer 2022).

Lidar-derived raster models are provided in bare-earth DEMs in *.tiff format and hillshade representations in *.pdf format. Processed aerial photographic bare-Earth DEMs are available in *.tiff format and hillshade models, and orthomosaics images are in *.pdf format. All *.pdf files contain information related to the survey and processing settings.

6. Discussion

6.1. Technical limitations

Our RPAS-borne surveys extend across much smaller areas than traditional airborne geophysical surveys, both due to Transport Canada regulations and battery capacity. Because of the Transport Canada requirement that an RPAS be in sight at all times, the size and location of our surveys were limited by the availability of cutblocks with minimal regrowth and in good post-logging condition rather than being guided by geological reasoning. An inherent limit when working in forested areas, the line-of-sight requirement would disappear when working in alpine areas or north of treeline in the Arctic. Nonetheless, the practical limit of battery capacity would remain.

Gamma-ray spectrometry will quantify K, eU, and eTh concentrations sourced from the top 30 cm of the Earth's surface. We acquired our data over subglacial tills, and thus variations in our measurements reflect changes in till matrix mineralogy and clast lithology. However, the organic and water content of surface soils can attenuate gamma radiation and may fluctuate on cm scales. Furthermore, near-surface cobble- to boulder-sized clasts embedded in till may influence readings. Thus, large-scale radiometric trends may be more representative of the overall till compositions than small-scale variations influenced by local organic and water content and near-surface clasts.

Table 8. Raw and processed output formats for each data type collected. A summary of parameters for each survey is provided in <BCGS_GF2023-07.zip>.

Type	Raw	Processed
Aerial photography		*.tiff (DEM), *.pdf (hillshade, orthomosaic)
Lidar		*.tiff (DEM), *.pdf (hillshade)
Radiometrics	*.csv (raw and processed points)	*.tiff, *.grd (K, eTh, eU, eTh/K, eU/eTh, eU/K)
Magnetics	*.csv (base station, magnetic total field)	*. csv (diurnal correction, tie line levelled), *.tiff, *.grd (total field, reduce to pole, vertical derivative)

6.2. Survey design

RPAS total field magnetic data are bulk measurements influenced by magnetic susceptibilities in bedrock and any overlying sediments. Future work will focus on separating total field measurements into bedrock and near-surface sediment components. For surveys where tie-lines were flown, and corrections could be made, significant changes in gridded data were not observed. In other words, our high-resolution, low-altitude, magnetics data that were acquired at a constant altitude above ground, can be confidently used with or without tie-line corrections. Rugged areas with steeper changes in topography would likely require tie lines to produce reliable results.

For most of the magnetic and radiometric surveys, a traverse line spacing of 5 or 10 m was used, and gridding at 1/3 line spacing (typical value for airborne geophysical data) produces a 1.67 or 3.33 m cell size. Higher resolution grids could be produced by flying tighter traverse lines. However, there are practical considerations to decreasing flight line spacing because more traverse lines will result in longer flight times and more battery changes. Also, global navigation satellite system base station corrections were not applied to magnetic and radiometric positional data and so tightly spaced flight lines would 'cross' in data plots when positional errors exceed flight line spacing.

6.3. Preliminary results and ongoing work

We are now completing work to relate measured RPAS magnetic and radiometric signatures to till samples and drift prospecting in the Interior Plateau. Preliminary results show that gridded RPAS magnetics and radiometrics products align with their traditional airborne equivalents. Variations within the total-field magnetics datasets match variations in traditional airborne data, reflecting the bulk magnetite content of signatures from bedrock and till combined. Potassium values associated with gridded RPAS-derived radiometric data conform with K values collected by traditional airborne and hand-held instruments. Lidar and photogrammetry products show mappable surficial geology at very high resolution and provide the ability to map ice flow landforms and features that are not visible in traditional aerial photographs. These products will be used in combination with stereo photos to identify small surficial geology units to aid interpreting drift prospecting datasets like RPAS-borne magnetics, radiometrics, and geochemical and mineralogical samples.

7. Summary

We completed 53 autopilot RPAS surveys over 13 areas in British Columbia's Interior Plateau. At each survey area, a DJI Matrice 600 Pro was used to collect airborne magnetic, radiometric, and lidar data. Magnetic and radiometric surveys were flown at heights from 5 to 10 m above ground level and at 1 to 2 m/s using active terrain-following guided by measurements from an onboard radar altimeter. Corrected magnetic and radiometric products are published at resolutions from 1.67 m cell size (at 5 m line spacing) to 3.33 m cell size (at 10 m line spacing). Lidar data were collected at 80 to 100 m above ground, at 4 m/s, producing 0.25 to 0.5 m/pixel resolution bare-earth DEMs. A Phantom 4 Pro RTK aircraft captured airborne RGB images at each area, which were processed using the structure-from-motion photogrammetric technique. Resultant point clouds were used to produce 0.1 m resolution DEMs and <0.03 m orthomosaic images. Forthcoming publications will assess the validity of the results presented herein by comparing them to traditional airborne radiometric and magnetic data, ground magnetic susceptibility and radiometric data, and to till sampling. These publications will also address the utility of RPAS-derived data in mapping surficial geology, interpreting ice-flow history, identifying areas for till sampling, and documenting dispersal trains down-ice from sites of in situ mineralization.

Acknowledgements

We thank W. Morton and B. Laird (Consolidated Woodjam Copper Corp.), J. Miller-Tait, C. Rees, and G. Roste (Mount Polley Mining and Imperial Metals corporations), and M. Cathro and G. Newton (Happy Creek Minerals Ltd.), for access to properties and insights into local geology. R. Bell (Drone Geoscience LLCFi), K. Linkevičs and A. Dobrovolskiy (SPH Engineering) provided technical advice and support about survey design and implementation. We greatly appreciate the instrument rentals and technical support provided by Terraplus Inc. (magnetometers), Candrone (lidar), and Radiations Solutions Inc. (gamma-ray spectrometer). A special thanks go to M. Sakals (British Columbia Ministry of Forests, Lands, Natural Resource Operations) and J. Thompson (British Columbia Ministry of Water, Land, and Resource Stewardship) for their guidance and knowledge in adopting remotely piloted aircraft systems into our field surveys. J. Van Der Vlugt, K. Zaborniak, and C. Fielding assisted capably in the office and the field. K. McLaren provided insightful comments to the lidar and photogrammetry sections and L. Aspler reviewed the manuscript.

References cited

Aleshin, I.M., Ivanov, S.D., Koryagin, V.N., Matveev, M.A., Morozov, Yu.A., Perederin, F.V., and Kholodkov, K.I., 2020. Review on the use of light unmanned aerial vehicles in geological and geophysical research. Seismic Instruments, 56, 509–515. <https://doi.org/10.3103/S0747923920050035>

Alsadik, B., and Remondino, F., 2020. Flight planning for lidar-based UAS mapping applications. ISPRS International Journal of Geo-Information, 9, 378p. <https://doi.org/10.3390/ijgi9060378>

Amestoy, J., Meslin, P.-Y., Richon, P., Delpuech, A., Derrien, S., Raynal, H., Pique, É., Baratoux, D., Chotard, P., Van Beek, P., Souhaut, M., and Zambardi, T., 2021. Effects of environmental factors on the monitoring of environmental radioactivity by airborne gamma-ray spectrometry. Journal of Environmental Radioactivity, 237, 12p. <https://doi.org/10.1016/j.jenvrad.2021.106695>

Arnold, H., Ferbey, T., and Hickin, A.S., 2016. Ice-flow indicator compilation, British Columbia and Yukon. British Columbia Ministry of Energy and Mines, British Columbia Geological Survey Open File 2016-04, 1:1,750,000 scale. <https://www2.gov.bc.ca/gov/content/industry/mineral-exploration-mining/british-columbia-geological-survey/geology/ice-flow-indicators>

Bellian, J.A., Kerans, C., and Jennette, D.C., 2005. Digital outcrop models: Applications of terrestrial scanning lidar technology in stratigraphic modeling. Journal of Sedimentary Research, 75, 166–176. <https://doi.org/10.2110/jsr.2005.013>

Bonneau, D.A., and Hutchinson, D.J., 2019. The use of terrestrial laser scanning for the characterization of a cliff-talus system in the Thompson River Valley, British Columbia, Canada Geomorphology, 327, 598–609. <https://doi.org/10.1016/j.geomorph.2018.11.022>

British Columbia Geological Survey, 2022. MINFILE. British Columbia Ministry of Energy, Mines and Petroleum Resources, British Columbia Geological Survey. (accessed December 2022). <https://www2.gov.bc.ca/gov/content/industry/mineral-exploration-mining/british-columbia-geological-survey/mineralinventory>

Brown, R., Gary, R., Janice, B., and Rees, C., 2016. Mount Polley Mine 2016 Technical Report. Imperial Metals Corporation. 205p. <https://imperialmetals.com/assets/docs/mount-polley-technical-report_may-20.2016.pdf>

Byrne, K., Stock, E., Ryan, J., Johnson, C., Nisenson, J., Jimenez, T.A., Stewart, H., Grubisa, G., and Sykora, S., 2013. Porphyry Cu-(Mo) deposits in the Highland Valley district, south-central British Columbia. In: Logan, J.M. and Schroeter, T.G., (Eds.), Porphyry Systems of central and southern BC: Prince George to Princeton. Society of Economic Geologists, Guidebook Series, 44, pp. 99–116.

Chabot, D., 2018. Trends in drone research and applications as the Journal of Unmanned Vehicle Systems turns five. Journal of Unmanned Vehicle Systems, 6, vi–xv. <https://doi.org/10.1139/juvs-2018-0005>

Clague, J.J., and Ward, B.C., 2011. Pleistocene glaciation of British Columbia. In: Ehlers, J., Gibbard, P.L., and Hughes, P.D. (Eds.) Developments in Quaternary Sciences Volume 15, pp. 563–573. <https://doi.org/10.1016/B978-0-444-53447-7.00044-1>

Clarke, G., Northcote, B., Corcoran, N., Heidarian H., and Hancock, K., 2023. Mines, mine development, selected proposed mines, and selected exploration projects in British Columbia. British Columbia Ministry of Energy, Mines and Low Carbon Innovation. British Columbia Geological Survey Open File 2023-01. <https://cmscontent.nrs.gov.bc.ca/geoscience/PublicationCatalogue/OpenFile/BCGS_OF2023-01.pdf>

D'Angelo, M., Miguel, A., Hollings, P., Byrne, K., Piercey, S., and Creaser, R.A., 2017. Petrogenesis and magmatic evolution of the Guichon Creek batholith: Highland Valley porphyry Cu ± (Mo) district, south-central British Columbia. Economic Geology, 112, 1857–1888. <https://doi.org/10.5382/econgeo.2017.4532>

Deblonde, C., Cocking, R.B., Kerr, D.E., Campbell, J.E., Eagles, S., Everett, D., Huntley, D.H., Inglis, E., Parent, M., Plouffe, A., Robertson, L., Smith, I.R., and Weatherston A., 2019. Surficial data model: the science language of the integrated Geological Survey of Canada data model for surficial geology maps. Geological Survey of Canada Open File 8236, 11p.

Demchuk, T.E., Ferbey, T., Kerr, B.J., and Levson, V.M., 2005. Surficial geology and aggregate potential mapping in northeast British Columbia using lidar imagery. In: Summary of Activities 2005, British Columbia Ministry of Energy and Mines, pp. 51-59.

Dent, D.L., MacMillan, R.A., Mayr, T.L., Chapman, W.K., and Berch, S.M., 2013. Use of airborne gamma radiometrics to infer soil properties for a forested area in British Columbia, Canada. Journal of Ecosystems and Management, 14, 12p. <https://doi.org/10.22230/jem.2013v14n1a201>

DJI, 2020. Phantom 4 RTK user manual v2.4. <https://dl.djicdn.com/downloads/phantom_4_rtk/20200721/Phantom_4_RTK_User_Manual_v2.4_EN.pdf>

DJI, 2022. Phantom 4 RTK, DJI Official. <https://www.dji.com/ca/phantom-4-rtk> (accessed March 2023).

Elia, E.A., and Ferbey, T., 2020. Generating photogrammetric DEMs in the field from remotely piloted aircraft systems. In: Geological Fieldwork 2019, British Columbia Ministry of Energy, Mines and Petroleum Resources, British Columbia Geological Survey Paper 2020-01, pp. 189-200.

Ferbey, T., and Elia, E.A., 2021. Preliminary surficial geology of the northern Hogem batholith area, north-central British Columbia. In: Geological Fieldwork 2020, British Columbia Ministry of Energy, Mines and Low Carbon Innovation, British Columbia Geological Survey Paper 2021-01, pp. 57-64.

Ferbey, T., Levson, V.M., and Plouffe, A., 2016a. Surficial geology, Moffat Creek area, British Columbia, parts of NTS 93-A/3, NTS 93-A/4, NTS 93-A/5, and NTS 93-A/6. British Columbia Ministry of Energy and Mines, British Columbia Geological Survey Geoscience Map 2016-01, 1:50,000 scale.

Ferbey, T., Plouffe, A., and Bustard, A.L., 2016b. Geochemical, mineralogical, and textural data from tills in the Highland Valley copper mine area, south-central British Columbia. British Columbia Geological Survey GeoFile 2016-11, Geological Survey of Canada Open File 8119, 15p. <https://doi:10.4095/299242>

Ford, K.L., Dilabio, R.N.W., and Rencz, A.N., 1988. Geological, geophysical and geochemical studies around the Allan Lake carbonatite, Algonquin Park, Ontario. Journal of Geochemical Exploration, 30, 99–121. <https://doi.org/10.1016/0375-6742(88)90054-4>

Francke, J., 2022. Advancements in ground penetrating radar technology for mineral exploration. Conference Abstract, Geoconvention 2022, Calgary, 5p. <https://geoconvention.com/wp-content/uploads/abstracts/2022/88888-advancements-in-ground-penetrating-radar-technology.pdf>

GEM Systems, 2023a. UAV sensors and components. <https://www.gemsys.ca/uav-magnetometers/> (accessed January 2023)

GEM Systems, 2023b. GEM GSM-19 Cost effective and high precision Overhauser magnetometer. <https://www.gemsys.ca/rugged-overhauser-magnetometer/> (accessed January 2023).

GeoBC, 2017. Specifications for digital elevation models for the province of British Columbia. Ministry of Forest, Lands and Natural Resources Operations, 2.2, 51p. <https://www2.gov.bc.ca/assets/gov/data/geographic/topography/elevation/geobc_dem_specifications.pdf>

Graden, R., 2013. NI 43-101 Technical Report Teck Highland Valley copper. Technical Report No. NI 43-101. Teck Resources Limited, 196p. <https://www.miningdataonline.com/reports/Highland%20Valley%20Copper_362013_TR.pdf>

Graham, D.F., and Bonham-Carter, G.F., 1993. Airborne radiometric data: A tool for reconnaissance geological mapping using a GIS. Photogrammetric Engineering & Remote Sensing, 59, 1243–1249.

Green Valley International, 2017. LiAir V70: UAV lidar system user guide. 41p. <https://greenvalleyintl.com/static/upload/file/20210716/1626437614111663.pdf >

Hashmi, S., 2015. Quaternary geology and drift prospecting in the Mount Polley region (NTS 093A). Unpublished M.Sc. thesis, Simon Fraser University, Burnaby, Canada, 165p. <https://summit.sfu.ca/item/15409>

Hashmi, S., Plouffe, A., and Ward, B.C., 2015a. Surficial geology of Bootjack Mountain area, parts of NTS 93-A/5, NTS 93-A/6, NTS 93-A/11, and NTS 93-A/12. Geological Survey of Canada Geoscience Map 2015-02, 1:50,000 scale.

Hashmi, S., Ward, B.C., Plouffe, A., Leybourne, M.I., and Ferbey, T., 2015b. Geochemical and mineralogical dispersal in till from the Mount Polley Cu-Au porphyry deposit, central British Columbia, Canada. Geochemistry: Exploration, Environment, Analysis, 15, 234–249. <https://doi.org/10.1144/geochem2014-310>

Haugerud, R.A., Harding, D.J., Johnson, S.Y., Harless, J.L., Weaver, C.S., and Sherrod, B.L., 2003. High-resolution lidar topography of the Puget Lowland, Washington —a bonanza for Earth science. GSA Today, 13, 4p. <https://doi.org/10.1130/1052-5173(2003)13<0004:HLTOTP>2.0.CO;2>

Holland, S.S., 1976. Landforms of British Columbia: a physiographic outline. In: British Columbia Ministry of Energy and Mines, and Petroleum Resources Bulletin 48, 138p.

Honarmand, M., and Shahriari, H., 2021. Geological mapping using drone-based photogrammetry: An application for exploration of vein-type Cu mineralization. Minerals, 11, 13p. <https://doi.org/10.3390/min11060585>

Hovgaard, J., and Grasty, R.L., 1997. Reducing statistical noise in airborne gamma-ray data through spectral component analysis. Proceedings of Exploration 97: Fourth Decennial International Conference on Mineral Exploration, 753–764.

Johnson, K., Nissen, E., Saripalli, S., Arrowsmith, J.R., McGarey, P., Scharer, K., Williams, P., and Blisniuk, K., 2014. Rapid mapping of ultrafine fault zone topography with structure from motion. Geosphere, 10, 969–986. <https://doi.org/10.1130/GES01017.1>

Kolster, M.E., Wigh, M.D., Lima Simões da Silva, E., Bjerg Vilhelmsen, T., and Døssing, A., 2022. High-speed magnetic surveying for unexploded ordnance using UAV systems. Remote Sensing, 14, 27p. <https://doi.org/10.3390/rs14051134>

Laird, B.L., 2017. Woodjam project summary report 2017. Technical Report. Consolidated Woodjam Copper Corp., 126p. < https://www.woodjamcopper.com/wp-content/uploads/2019/07/WJ_2017_Summary_Report.pdf>

Le Maire, P., Bertrand, L., Munschy, M., Diraison, M., and Géraud, Y., 2020. Aerial magnetic mapping with an unmanned aerial vehicle and a fluxgate magnetometer: a new method for rapid mapping and upscaling from the field to regional scale. Geophysical Prospecting, 68, 2307–2319. <https://doi.org/10.1111/1365-2478.12991>

Lemmens, M., 2007. Airborne Lidar Sensors. GIM International, Product Survey, 4p. < https://community.esri.com/ccqpr47374/attachments/ccqpr47374/gis-blog/507/1/LiDAR-Sensors.pdf >

Lesage, G., Byrne, K., Morris, W.A., Enkin, R.J., Lee, R.G., Mir, R., and Hart, J.R., 2019. Interpreting regional 3D fault networks from integrated geological and geophysical data sets: An example from the Guichon Creek batholith, British Columbia. Journal of Structural Geology, 119, 93-106.

Logan, J.M., and Mihalynuk, M.G., 2014. Tectonic controls on early Mesozoic paired alkaline porphyry deposit belts (Cu-Au Ag-Pt-Pd-Mo) within the Canadian Cordillera. Economic Geology, 109, 827–858. <https://doi.org/10.2113/econgeo.109.4.827>

Logan, J.M., Schiarizza, P., Struik, L.C., Barnett, C., Nelson, J.L., Kowalczyk, P., Ferri, F., Mihalynuk, M.G., Thomas, M.D., Gammon, P., Lett, R., Jackaman, W., and Ferbey, T., 2010. Bedrock geology of the QUEST map area, central British Columbia. British Columbia Ministry of Energy, Mines and Petroleum Resources, British Columbia Geological Survey Geoscience Map 2010-01, 1:500,000 scale.

Lohani, B., and Ghosh, S., 2017. Airborne LiDAR technology: A review of data collection and processing systems. Proceedings of the National Academy of Sciences, India Section A: Physical Sciences, 87, 567–579. <https://doi.org/10.1007/s40010-017-0435-9>

Maino, A., Alberi, M., Anceschi, E., Chiarelli, E., Cicala, L., Colonna, T., De Cesare, M., Guastaldi, E., Lopane, N., Mantovani, F., Marcialis, M., Martini, N., Montuschi, M., Piccioli, S., Raptis, K.G.C., Russo, A., Semenza, F., and Strati, V., 2022. Airborne radiometric surveys and machine learning algorithms for revealing soil texture. Remote Sensing, 14, 16p. <https://doi.org/10.3390/rs14153814>

Malehmir, A., Dynesius, L., Paulusson, K., Paulusson, A., Johansson, H., Bastani, M., Wedmark, M., and Marsden, P., 2017. The potential of rotary-wing UAV-based magnetic surveys for mineral exploration: A case study from central Sweden. The Leading Edge, 36, 552–557. <https://doi.org/10.1190/tle36070552.1>

Martin, P.G., Payton, O.D., Fardoulis, J.S., Richards, D.A., and Scott, T.B., 2015. The use of unmanned aerial systems for the mapping of legacy uranium mines. Journal of Environmental Radioactivity, 143, 135–140. <https://doi.org/10.1016/j.jenvrad.2015.02.004>

Martin, P.G., Connor, D.T., Estrada, N., El-Turke, A., Megson-Smith, D., Jones, C.P., Kreamer, D.K., and Scott, T.B., 2020. Radiological Identification of near-surface mineralogical deposits using low-altitude unmanned aerial vehicle. Remote Sensing, 12, 17p. <https://doi.org/10.3390/rs12213562>

McClenaghan, M.B., and Paulen, R.C., 2017. Application of till mineralogy and geochemistry to mineral exploration. In: Menzies, J. and van der Meer, J.J.M., (Eds.), Past Glacial Environments. Elsevier, 2, pp. 689–751. <https://doi.org/10.1016/B978-0-08-100524-8.00022-1>

McClenaghan, M.B., Plouffe, A., McMartin, I., Campbell, J.E., Spirito, W.A., Paulen, R.C., Garrett, R.G., and Hall, G.E.M., 2013. Till sampling and geochemical analytical protocols used by the Geological Survey of Canada. Geochemistry: Exploration, Environment, Analysis, 13, 285–301. <https://doi.org/10.1144/geochem2011-083>

McGregor, D.S., 2018. Materials for gamma-ray spectrometers: Inorganic scintillators. Annual Review of Materials Research, 48, 245–277. <https://doi.org/10.1146/annurev-matsci-070616-124247>

Minty, B., and Hovgaard, J., 2002. Reducing noise in gamma-ray spectrometry using spectral component analysis. Exploration Geophysics, 33, 172–176. <https://doi.org/10.1071/EG02172>

Maune, D.F., Heidemann, H.K., Kopp, S.M., and Crawford, C.A., 2018. Introduction to digital elevation models. In: Maune, D.F., Nayegandhi, A.. (Eds.), Digital Elevation Model Technologies and Applications: The Dem Users Manual 3rd Edition. 3, pp. 1-40.

Nabighian, M.N., Grauch, V.J.S., Hansen, R.O., LaFehr, T.R., Li, Y., Peirce, J.W., Phillips, J.D., and Ruder, M.E., 2005. The historical development of the magnetic method in exploration. GEOPHYSICS, 70, 33ND-61ND. <https://doi.org/10.1190/1.2133784>

Nayegandhi, A., Nimetz, J., 2018. Airborne topographic lidar. In: Maune, D.F., Nayegandhi, A. (Eds.), Digital Elevation Model Technologies and Applications: The Dem Users Manual 3rd Edition. 3, pp. 205-236.

Nesbit, P.R., Durkin, P.R., Hugenholtz, C.H., Hubbard, S.M., and Kucharczyk, M., 2018. 3-D stratigraphic mapping using a digital outcrop model derived from UAV images and structure-from-motion photogrammetry. Geosphere, 14, 2469-2486. <https://doi.org/10.1130/GES01688.1>

Ney, C.S., Anderson, J.M., and Panteleyev, A., 1972. Discovery, geologic setting and style of mineralization, Sam Goosly deposit, B.C. CIM Bulletin, July 1972, 53–64.

O'Reilly, G.A., and Ford, K.L., 1988. The role of airborne gamma-ray spectrometry in bedrock mapping and mineral exploration: case studies from granitic rocks within the Meguma zone, Nova Scotia. Maritime Sediments and Atlantic Geology, 24, 47–60.

Pisiak, L.K., Canil, D., Grondahl, C., Plouffe, A., Ferbey, T., and Anderson, R.G., 2014. Magnetite as a porphyry copper indicator mineral in till: A test using the Mount Polley porphyry copper-gold deposit, south-central British Columbia (NTS 093A). In: Geoscience BC Summary of Activities 2014, Geoscience BC, Report 2015-1, pp. 141-150.

Plouffe, A. and Ferbey, T., 2016. Till geochemistry, mineralogy and textural data near four Cu porphyry deposits in British Columbia. Geological Survey of Canada, Open File 8038, British Columbia Ministry of Energy and Mines, British Columbia Geological Survey, GeoFile 2016-10.

Plouffe, A., and Ferbey, T., 2018. Surficial geology of the Highland Valley copper mine area (Parts of NTS 092I/06, 7, 10 and 11), British Columbia., British Columbia Ministry of Energy and Mines, British Columbia Geological Survey Geoscience Map 2018-01, 1:50,000 scale.

Porter, J.K., and Lowe, C., 2000. Airborne gamma-ray spectrometry over the Endako porphyry molybdenum district in central British Columbia. Geological Survey of Canada, Current Research 2000-E2, 9p. <https://doi.org/10.4095/211509>

Rees, C. 2013. The Mount Polley Cu-Au porphyry deposit, south-central British Columbia, Canada. In: Logan, J.M. and Schroeter, T.G., (Eds.), Porphyry Systems of central and southern BC: Prince George to Princeton. Society of Economic Geologists, Guidebook Series, 44, pp. 67–98.

Sahoo, H., and Gani, N.D., 2015. Creating three-dimensional channel bodies in LiDAR-integrated outcrop characterization: A new approach for improved stratigraphic analysis. Geosphere, 11, 777–785. <https://doi.org/10.1130/GES01075.1>

TsTsukj, O., Matolín, M., and Gryc, L., 2018. Mapping of radiation anomalies using UAV mini-airborne gamma-ray spectrometry. Journal of Environmental Radioactivity, 182, 101–107. <https://doi.org/10.1016/j.jenvrad.2017.11.033>

Sappin, A.-A., Dupuis, C., Beaudoin, G., Pozza, M., McMartin, I., and McClenaghan, M.B., 2014. Optimal ferromagnetic fraction in till samples along ice-flow paths: case studies from the Sue-Dianne and Thompson deposits, Canada. Geochemistry: Exploration, Environment, Analysis, 14, 315–329. <https://doi.org/10.1144/geochem2013-212>

Schiarizza, P., and Church, N., 1996. The geology of the Thompson – Okanagan mineral assessment region. British Columbia Ministry of Energy, Mines and Petroleum Resources, British Columbia Geological Survey Open File 1996-20.

Sherlock, R., Poos, S., and Trueman, A., 2012. NI 43-101 Technical Report for 2011 Activities on the Woodjam South Property. Gold Fields Horsefly Exploration Corp., Consolidated Woodjam Copper Corporation, 194 p. <https://woodjamcopper.com/data/NI%2043-101%20Woodjam%20Technical%20Report.pdf >

Sherlock, R., Blackwell, J., and Skinner, T., 2013. NI 43-101 Technical Report for 2012 Activities on the Woodjam North Property. Gold Fields Horsefly Exploration Corp., Consolidated Woodjam Copper Corporation, 285p. < https://minehutte.com/content/uploads/2015/02/Canada-British-Columbia-Consolidated-Woodjam-Copper-Corp-Woodjam-North-Property-Gold-Fields-Exploration-Inc-May2013.pdf >

Shives, R.B.K., 2015. Using gamma ray spectrometry to find rare metals. In: Simandl, G.J. and Neetz, M., (Eds.), Symposium on Strategic and Critical Materials Proceedings, November 13-14, 2015, Victoria, British Columbia. British Columbia Ministry of Energy and Mines, British Columbia Geological Survey Paper 2015-3, pp. 199-209.

Shives, R.B.K., Holman, P.B., Rebolledo, L., and Hetu, R.J., 1995. Airborne geophysical survey: Mount Polley area, B.C., Geological Survey of Canada Open File 2802, 66p.

Shives, R.B.K., Charbonneau, B.W., and Ford, K.L., 2000. The detection of potassic alteration by gamma-ray spectrometry—Recognition of alteration related to mineralization. Geophysics, 65, 2001–2011. <https://doi.org/10.1190/1.1444884>

Shives, R.B.K., Carson, J.M., Dumont, R., Ford, K.L., Holman, P.B., and Cathro, M., 2004. Helicopter-borne gamma ray spectrometric and magnetic total field geophysical survey Imperial Metals Corporation's Mount Polley mine area, British Columbia (Part of NTS 93A/12). Geological Survey of Canada Open File 4619.

Smith, Z.D., and Maxwell, D.J., 2021. Constructing vertical measurement logs using UAV-based photogrammetry: Applications for multiscale high-resolution analysis of coarse-grained volcaniclastic stratigraphy. Journal of Volcanology and Geothermal Research, 409, 20p. <https://doi.org/10.1016/j.jvolgeores.2020.107122>

Spence, D.W., Crawford, H., Scoates, J.S., Nott, J.A., Nixon, G.T., and Milidragovic, D., 2022. Mapping ultramafic cumulates at the Tulameen ultramafic-mafic Alaskan-type intrusion, south-central British Columbia, aided by remotely piloted aircraft system photogrammetry. In: Geological Fieldwork 2021, British Columbia Ministry of Energy, Mines and Low Carbon Innovation, British Columbia Geological Survey Paper 2022-01, pp. 103-122.

Tammenmaa, J., Grasty, R.L., and Peltoniemi, M., 1976. The reduction of statistical noise in airborne radiometric data. Canadian Journal of Earth Sciences, 13, 1351–1357. <https://doi.org/10.1139/e76-140>

Telford, W.M., Geldart, L.P., and Sheriff, R.E., 1989. Applied geophysics, 2nd ed. Cambridge University Press, 750p.

Transport Canada, 2022. Aeronautical information manual (AIM). <https://tc.canada.ca/sites/default/files/2022-09/aim-2022-2_access_e.pdf>

Tsuji, T., Kinoshita, J., Tsuji, S., Yamamoto, K., and Ikeda, T., 2021. Drone-based active-source multichannel seismic survey system. Summit on Drone Geophysics 2021. Society of Exploration Geophysicists, p. 30. <https://seg.org/Portals/0/OpenContent/Files/9503/2021_Summit_on_Drone_Geophysics_-_Program_Booklet.pdf>

UgCS, 2023. Drone flight planning and control software by SPH Engineering. <https://www.ugcs.com> (accessed January 2023).

Vandekerkhove, S., Rowins, S.M., and Johnston, S.T., 2014. Geology and physicochemical conditions of copper-gold mineralization at the Three Firs porphyry prospect, Woodjam district, south-central British Columbia. In: Geological Fieldwork 2013, British Columbia Ministry of Energy and Mines, British Columbia Geological Survey Paper 2014-1, pp. 67-94.

van der Veeke, S., Limburg, J., Koomans, R.L., Söderström, M., and van der Graaf, E.R., 2021. Optimizing gamma-ray spectrometers for UAV-borne surveys with geophysical applications. Journal of Environmental Radioactivity, 237, 14p. <https://doi.org/10.1016/j.jenvrad.2021.106717>

Vollgger, S.A., and Cruden, A.R., 2016. Mapping folds and fractures in basement and cover rocks using UAV photogrammetry, Cape Liptrap and Cape Paterson, Victoria, Australia. Journal of Structural Geology, 85, 168–187. <https://doi.org/10.1016/j.jsg.2016.02.012>

Weiner, S., Wu, X., Pagel, Z., Li, D., Sleczkowski, J., Ketcham, F., and Mueller, H., 2020. A flight capable atomic gravity gradiometer with a single laser. 2020 IEEE International Symposium on Inertial Sensors and Systems (INERTIAL), Hiroshima, Japan, 1–3. <https://doi.org/10.1109/INERTIAL48129.2020.9090014>

BRITISH COLUMBIA

Ministry of
Energy, Mines and
Low Carbon Innovation

BRITISH COLUMBIA
est. 1895
GEOLOGICAL SURVEY